A Multiscale Observational Case Study of a Pacific Atmospheric River Exhibiting Tropical–Extratropical Connections and a Mesoscale Frontal Wave

F. MARTIN RALPH, PAUL J. NEIMAN, GEORGE N. KILADIS, AND KLAUS WEICKMANN

NOAA/Earth System Research Laboratory/Physical Sciences Division, Boulder, Colorado

DAVID W. REYNOLDS

NOAA/National Weather Service/WFO San Francisco Bay Area, Monterey, California

(Manuscript received 17 August 2010, in final form 28 October 2010)

ABSTRACT

A case study is presented of an atmospheric river (AR) that produced heavy precipitation in the U.S. Pacific Northwest during March 2005. The study documents several key ingredients from the planetary scale to the mesoscale that contributed to the extreme nature of this event. The multiscale analysis uses unique experimental data collected by the National Oceanic and Atmospheric Administration (NOAA) P-3 aircraft operated from Hawaii, coastal wind profiler and global positioning system (GPS) meteorological stations in Oregon, and satellite and global reanalysis data. Moving from larger scales to smaller scales, the primary findings of this study are as follow: 1) phasing of several major planetary-scale phenomena influenced by tropical–extratropical interactions led to the direct entrainment of tropical water vapor into the AR near Hawaii, 2) dropsonde observations documented the northward advection of tropical water vapor into the subtropical extension of the midlatitude AR, and 3) a mesoscale frontal wave increased the duration of AR conditions at landfall in the Pacific Northwest.

1. Introduction

Extreme precipitation on the U.S. west coast presents at least two major practical challenges that serve as motivation for the study presented here. First, protection of life and property in floods requires the accurate prediction of the timing, location, and intensity of extreme precipitation and runoff on the scales of key watersheds. Adequate lead time is needed to prepare, for example, to evacuate people hours to days before a flood (e.g., Ralph et al. 2003) or, potentially, to draw down reservoirs days to weeks before an extreme event. Second, policies that affect major economic sectors, such as housing (Dettinger et al. 2009), require climate change projections of extreme precipitation and flooding events as policy makers consider major changes to flood control and water supply infrastructure (e.g., dams–reservoirs, levees). As highlighted by the Dettinger et al. (2009) study and by Ralph et al. (2010), uncertainties in climate projections and errors in quantitative precipitation forecasts (QPFs) are significant. As a step toward addressing these challenges, the current study examines a uniquely well-observed extreme precipitation event to better understand the role of atmospheric river (AR) conditions, and how they were affected by planetary-scale, synoptic-scale, and mesoscale physical processes.

ARs are a phenomenon that is key to both the global water cycle (e.g., Zhu and Newell 1998), and to extreme precipitation and flooding (e.g., Ralph et al. 2006; Stohl et al. 2008; Leung and Qian 2009; Knippertz and Wernli 2010). ARs play a key role in horizontal water vapor transport and, yet, are relatively narrow filaments (i.e., ''rivers'') roughly 400 km wide on average (Ralph et al. 2004) that perform >90% of the horizontal water vapor transport in midlatitudes (Zhu and Newell 1998). Also, their characteristics are ideal for creating strong orographic precipitation when they encounter terrain (Neiman et al. 2002, 2008b; Ralph et al. 2005a; Falvey and Garreaud 2007; Smith et al. 2010). When AR conditions occur, they are located in the warm sector of extratropical cyclones and can be characterized by strong winds and

Corresponding author address: F. Martin Ralph, NOAA/Earth System Research Laboratory/Physical Sciences Division, Mail Code R/PSD2, 325 Broadway, Boulder, CO 80305.
E-mail: marty.ralph@noaa.gov

DOI: 10.1175/2010MWR3596.1

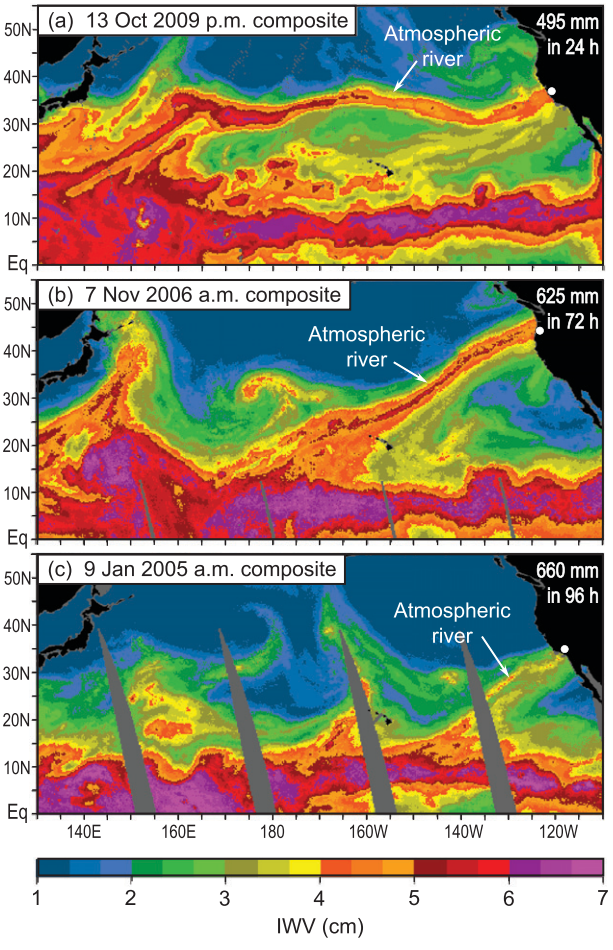

FIG. 1. Examples of AR events that produced extreme precipitation along the U.S. west coast, and exhibited spatial continuity with the tropical water vapor reservoir as seen in SSM/I satellite observations of IWV. Composite SSM/I satellite images of IWV (cm) of an AR emanating from the tropical (a) western Pacific on the afternoon of 13 Oct 2009, (b) central Pacific on the morning of 7 Nov 2006 (see Neiman et al. 2008a for a detailed summary), and (c) eastern Pacific on the morning of 9 Jan 2005. The images were generated using the algorithm of Wentz (1995).

large water vapor contents at low altitudes (Ralph et al. 2004, 2005a). They constitute the part of the warm conveyor belt (e.g., Browning 1990; Carlson 1991) containing strong latent heat transport. Figure 1 shows three examples of ARs observed using measurements of vertically integrated water vapor (IWV) from Special Sensor Microwave Imager (SSM/I) (Hollinger et al. 1990) satellite measurements. In each of these cases, extreme precipitation occurred somewhere along the U.S. west coast, ranging from 495 mm in less than a day to 660 mm in 4 days, including the November 2006 event (Fig. 1b) documented by Neiman et al. (2008a). The temporal evolution of one event, the one studied in detail in this paper, is shown in Fig. 2. The AR developed first near Hawaii (Fig. 2a) and then struck the U.S. west coast (Fig. 2c), which led to heavy orographic precipitation (Fig. 2e) and high stream flows that brought an end to a period of drought in the Pacific Northwest. (It is important to recognize that while a static image of an AR, as in Figs. 1 and 2, suggests that an Eulerian perspective can be helpful, the Lagrangian nature of the water vapor transport in ARs is a crucial concept that better represents the fact that rainout, evaporation, moisture convergence, and other processes modulate the water vapor transport along an AR.) An underlying question is, what conditions, from the planetary to the mesoscale, are important for distinguishing average ARs from those that produce extreme rainfall or flooding?

A number of studies of related phenomena provide context for this paper. On the planetary scale, research has identified linkages between tropical forcing and the baroclinic waves and storm track that bring precipitation to the U.S. west coast. Mo and Higgins (1998a,b) showed that the location of tropical convection in the Pacific modulates water vapor transport at midlatitudes, affecting the U.S. west coast. Mo (1999), as well as Bond and Vecchi (2003), documented correlations between the position of the Madden–Julian oscillation (MJO) in the tropics and alternating wet and dry episodes along the West Coast. Jones (2000) showed that the best correlation to extreme precipitation in California was when MJO convection was positioned over the Indian Ocean. Kiladis (1998) diagnosed linkages between tropical convection, subtropical moisture flux, and extratropical Rossby waves. Within this context, the presence of two parallel ARs in the North Pacific in Fig. 2 is strongly suggestive of such tilted extratropical wave packets (EWPs), which advect moisture poleward along the leading edges of upper-level troughs and associated surface fronts. Shapiro et al. (2001) explored the modulating effect of the El Niño–Southern Oscillation (ENSO) on key characteristics of EWPs (Chang 1993; Chang 2005) in the eastern Pacific. These studies and many others on the links between tropical forcing, EWPs, and storm tracks are summarized in Dole (2008).

An important direct tropical–extratropical interaction that is characteristic of at least some ARs that produce extreme precipitation is that they extend to the tropics and apparently entrain, or ''tap,'' tropical moisture, which can then be advected to higher latitudes. This inference is based on SSM/I IWV satellite imagery (e.g., Figs. 1 and 2), selected case studies (Neiman et al. 2008a; Leung and Qian 2009), and model trajectory analysis (Bao et al. 2006; Stohl et al. 2008; Knippertz and Wernli 2010). Knippertz and Martin (2007) also explored the subject of water vapor transport from the tropics to subtropics, but in cutoff lows where midtropospheric (700 mb) water vapor transport defined what they termed a moist conveyor belt. However, direct observation of water vapor transport

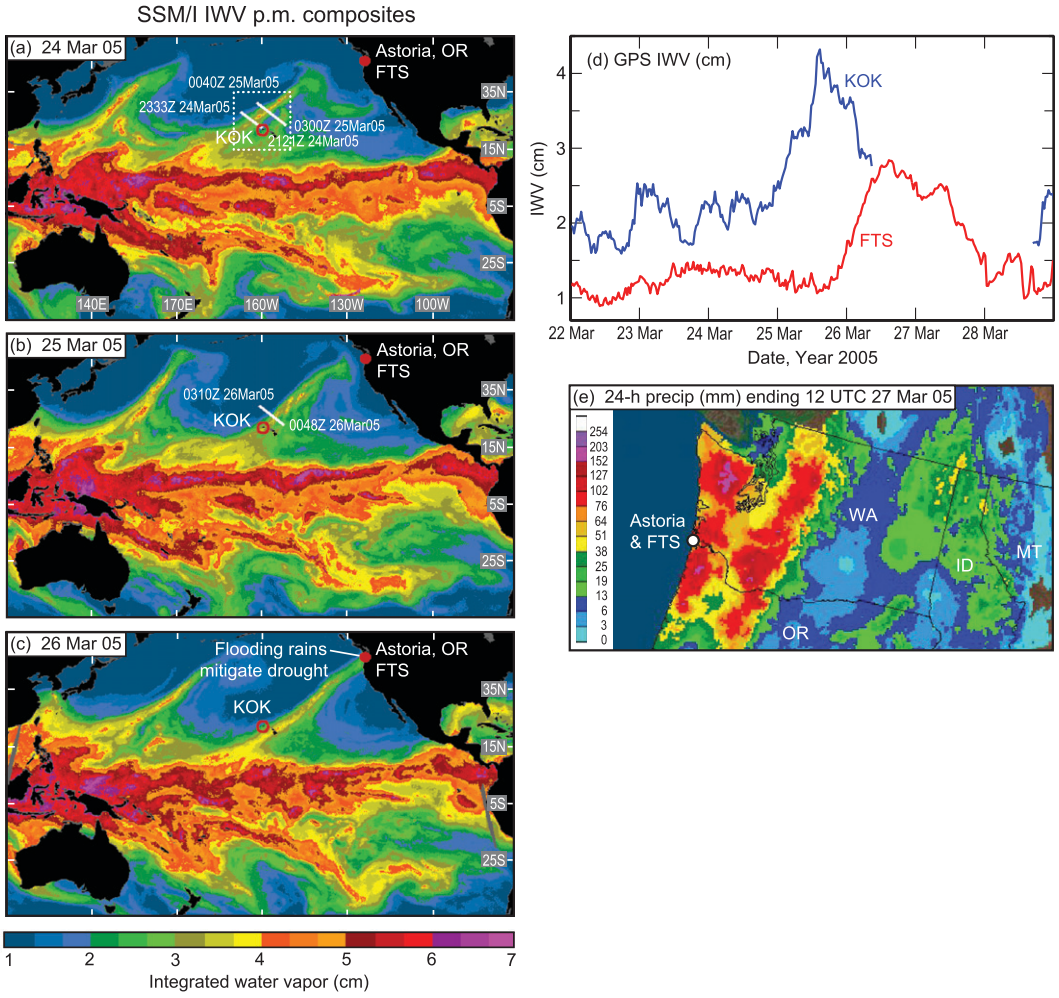

FIG. 2. Composite SSM/I satellite imagery of IWV (cm; color bar at bottom) constructed from polar-orbiting swaths between ~1200 and 2359 UTC on (a) 24, (b) 25, and (c) 26 Mar 2005. The wind profiler site at AST and the GPS sites at nearby FTS (red dot) and KOK (red circle) are shown. The white lines in (a) and (b) portray time-to-space-adjusted NOAA P-3 dropsonde curtains, with date and time end points shown. The white dotted inset box in (a) is the domain for Fig. 7. (d) Time series of IWV (cm) measured by GPS receivers at KOK (blue) and FTS (red). (e) Analysis of the 24-h QPE (mm) ending 12 UTC 27 Mar 2005 across the Pacific Northwest, from NOAA's Advanced Hydrologic Prediction Service. The boldface white dot shows the locations of Astoria and FTS.

near the key interface between the tropics and subtropics in an AR event has not been possible in the past. This study uses dropsonde and in situ data from National Oceanic and Atmospheric Administration (NOAA) P-3 aircraft flights operated out of Hawaii, as well as satellite and reanalysis data, to start to fill this gap.

Once the planetary- and synoptic-scale conditions are established, the mesoscale details of the AR, its parent extratropical cyclone, mesoscale precipitation processes, and the local terrain ultimately determine which watersheds will receive the most precipitation. These mesoscale details are crucial to forecasting and to mitigation of flood risks through early warning. This fact, and the related requirements, have led to the establishment of the Hydrometeorology Testbed (HMT), which has been focused on extreme precipitation events along the U.S. west coast (Ralph et al. 2005b), and the challenge of making accurate QPFs (Ralph et al. 2010). Several HMT-related studies of QPF methods have developed and evaluated advanced approaches for numerical models (Jankov et al. 2007; Junker et al. 2008; Yuan et al. 2008; Ma et al. 2011). In addition, detailed analyses of an extreme event in California by Ralph et al. (2003) and Neiman et al. (2004) have documented the presence of a meso-alpha-scale frontal wave of roughly 500–1000-km horizontal wavelength along the primary cold front. Their studies, as well as forecaster experience (Morss and Ralph 2007), have noted the importance of the low-level jet (LLJ) ahead of the primary cold front in these storms in terms of predicting floods in California. Earlier studies in Europe

and New Zealand (Wratt et al. 1996) centered on the warm sector and the LLJ in focusing orographic precipitation (e.g., Browning et al. 1974) and in creating damaging winds (Crochet et al. 1990). This region of the storm has now been recognized as representing AR conditions, and since the frontal waves modulate the characteristics of the front and its associated AR (position, strength, propagation, vertical motion), it is crucial to determine which watersheds are likely to flood (Ralph et al. 2003; Andrews et al. 2004). However, none of these earlier studies has clearly documented the connection between the impacts of frontal wave variations on an AR and the resulting focusing of extreme rainfall into a relatively small area. This gap is addressed through the case study presented herein and development of a conceptual model focused on how the mesoscale frontal wave affects the duration of AR conditions along the coast [note that duration was identified by Doswell et al. (1996) as a key factor in flash flood prediction].

Because this paper presents a detailed case study, based largely on the availability of unique experimental data, the results are not to be interpreted as representative of all extreme precipitation events along the U.S. west coast, but rather as illustrative of one unusually well-documented case. Each of the three examples of ARs shown in Fig. 1 appears to have a direct connection to the tropical water vapor reservoir, and each produced extreme precipitation on the U.S. west coast. Although each event exhibits the patterns in IWV characteristic of ARs that were identified in Ralph et al. (2004, 2005a) and Neiman et al. (2008b), and each shows a pattern suggestive of entrainment of tropical water vapor into the subtropical extensions of these ARs, their ''connection'' to the tropical IWV reservoir occurs in different geographical regions, that is, the western Pacific (Fig. 1a), central Pacific (Fig. 1b), and the eastern Pacific (Fig. 1c), and under differing synoptic-scale patterns (not shown). It is important to note that the interpretations of the midlatitude IWV patterns (as in Figs. 1 and 2) as being indicative of strong water vapor transport in ARs were verified using research aircraft data in Ralph et al. (2004, 2005a) and using global reanalysis data in Neiman et al. (2008b). However, interpretations of IWV patterns in or near the tropics are not as straightforward, which is one of the gaps the unique P-3 aircraft data address in this paper. While a detailed compositing study of many such events is a desirable goal, it is beyond the scope of this detailed case study and, thus, will be the focus of future work.

2. Key datasets

This study focuses on the northern and tropical Pacific basin, a large area with sparse in situ observations. Hence, operational satellite observations were used to provide remotely sensed datasets across this region in March and April 2005. During this period, an SSM/I (Hollinger et al. 1990) was carried on each of three Defense Meteorological Satellite Program polar-orbiting satellites with sampling that was asynoptic and irregular in time and location, and available only over the ocean. IWV retrievals were composited onto a 0.25° (~25 km) latitude–longitude grid of the ascending and descending satellite passes for each day, providing nearly complete spatial sampling across the basin. The IWV (Schluessel and Emery 1990), cloud liquid water (CLW; Weng and Grody 1994), and rain rate (Ferriday and Avery 1994) were retrieved from the SSM/I sensors. In addition to the polar orbiters, geosynchronous satellites recorded multichannel data globally, including surface and/or cloud-top brightness temperatures T_b. NOAA's *Geostationary Operational Environmental Satellite-10* (*GOES-10*) provided coverage across the Pacific Ocean east of ~165°E. Observations of T_b from merged, time-synchronous geostationary and polar-orbiting satellite observations were used to generate the Cloud Archive User Services (CLAUS) dataset, which is available globally 8 times daily at 0.5° resolution (e.g., Hodges et al. 2000). This dataset serves as an indicator for upper-level cold cloudiness, and a good proxy for deep convection within the tropics. A volumetric representation of the large-scale meteorological conditions was achieved using the 4 times per day relatively coarse resolution (~2.5° latitude × ~2.5° longitude) global gridded dataset from the National Centers for Environmental Prediction–National Center for Atmospheric Research (NCEP–NCAR) reanalysis project (Kalnay et al. 1996).

To obtain a much more detailed depiction of atmospheric conditions, albeit over a comparatively limited spatiotemporal domain over the subtropical eastern Pacific, a NOAA P-3 research aircraft flew two key missions out of Honolulu, Hawaii, in late March 2005. During each flight, the P-3 recorded standard meteorological parameters every 1 s from ~300 m above the ocean surface upward to ~400 hPa. The two missions were carried out between 2050 UTC 24 March and 0433 UTC 25 March and between 2035 UTC 25 March and 0455 UTC 26 March. Mission 1 released 44 GPS dropsondes in two curtains (Fig. 2a), while mission 2 released 23 GPS dropsondes in a single curtain (Fig. 2b). These dropsondes provided high-resolution vertical profiles of wind velocity, temperature, and water vapor. A lower-fuselage scanning C-band (~5.6-cm wavelength) radar recorded precipitation reflectivity data.

A suite of land-based experimental and operational observing systems that gathered data over northwestern

Oregon during late March 2005 are used. A NOAA/Earth System Research Laboratory/Physical Sciences Division (NOAA/ESRL/PSD) all-weather 915-MHz radar wind profiler along the coast at Astoria, Oregon (AST; 3 m MSL), provided hourly averaged vertical profiles of horizontal wind from ~0.1 to 5.0 km above ground level with ~100-m vertical resolution and ~1 m s^{-1} accuracy (e.g., Carter et al. 1995). The profiler winds were objectively edited using the time–height continuity method of Weber et al. (1993). The height of the precipitation melting level was determined objectively using the brightband detection method of White et al. (2002). A collocated tipping-bucket rain gauge measured rainfall with 0.01-in. (~0.25 mm) resolution, while on-site observations of wind, temperature, water vapor, and pressure were collected from a 10-m tower, all with 2-min sampling. At nearby Fort Stevens, Oregon (FTS; 10 m MSL), 30-min measurements of IWV in the full atmospheric column above a dual-frequency GPS receiver were retrieved with ~1-mm accuracy by measuring the apparent delays in the arrival of radio signals transmitted by the constellation of GPS satellites (e.g., Duan et al. 1996; Mattioli et al. 2007). This study utilizes additional GPS IWV data collected from Salem, Oregon (SLE; 76 m MSL), and from Kokole, Hawaii (KOK; 7 m MSL; see Fig. 2). A remote automated weather station provided hourly rainfall observations in the coastal mountains of northwestern Oregon at South Fork (SFK; 688 m MSL), while a nearby U.S. Geological Survey (USGS) stream gauge recorded data near the mouth of Nehalem River at Foss (FSS; 10 m MSL).

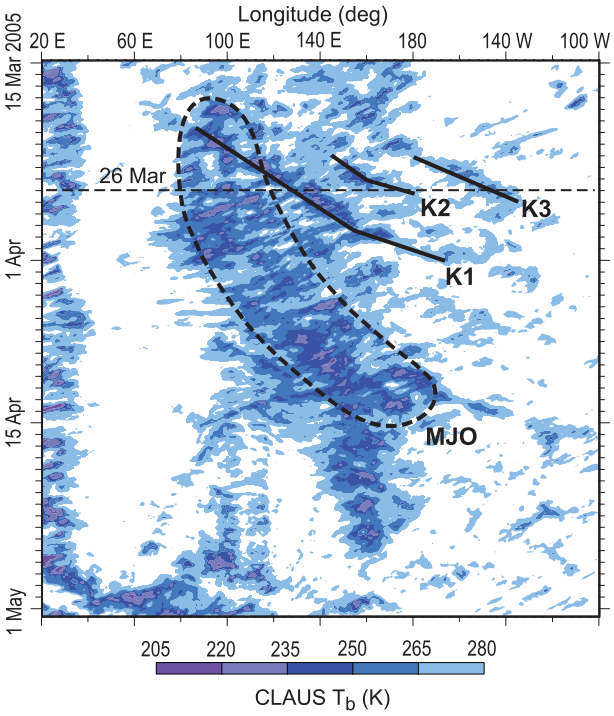

FIG. 3. Time–latitude diagram of CLAUS brightness temperatures (T_b; K) for the period 15 Mar–2 May 2005, averaged between 5°N and 5°S over a longitude range extending from eastern Africa on the left to the coast of central America. Lower T_b signifies cold upper-tropospheric cloud associated with deep convective systems, which are organized into multiple time and space scales. Three Kelvin waves (K1–K3) are emphasized with boldface lines, and a strong MJO is enclosed by the dashed line. The horizontal dashed line corresponds to 26 Mar 2005.

3. Planetary-scale perspective

Dole (2008) provides a useful summary of key mechanisms linking short-term variability in the extratropical storm track to tropical convection and related forcing mechanisms that were active during this event. While many of these mechanisms have been robustly identified statistically in observations, it is of course more difficult to prove causality in individual cases. This study links many of the well-established dynamical mechanisms shown in previous studies to the evolution of a particular AR. Bearing in mind that AR events may originate through a wide variety of large-scale flow patterns over the Pacific, this case represents one scenario of how such tropical–extratropical linkages can lead to extreme precipitation in North America.

In Fig. 2, SSM/I imagery displays a connection in IWV between the flood event across the Pacific Northwest and deep moisture regions within the near-equatorial intertropical convergence zone (ITCZ) over the central Pacific. Such connections have been well documented for atmospheric rivers affecting the west coast of North America (e.g., Ralph et al. 2004; Neiman et al. 2008a,b). Wave energy propagating into the equatorial east Pacific from the extratropics is common over the central and eastern Pacific domain during northern winter and spring (Kiladis and Weickmann 1992; Kiladis 1998; Mo 1999), but its amplitude and path are strongly influenced by the large-scale basic state.

A Hovmöller diagram of CLAUS brightness temperatures in Fig. 3 (averaged between 5°N and 5°S) shows that the tropical convection field during the study period was dominated by the occurrence of an MJO convective envelope, with an envelope of enhanced convection amplifying over the Indian Ocean during mid-March, then moving eastward into the western Pacific at around 5 m s^{-1}, consistent with a typical MJO event (e.g., Zhang 2005). Embedded within and to the east of the MJO convection are several faster convective envelopes propagating eastward at phase speeds closer to 15 m s^{-1} (labeled K1, K2, and K3), having characteristics of convectively coupled Kelvin waves as revealed by space–time filtering

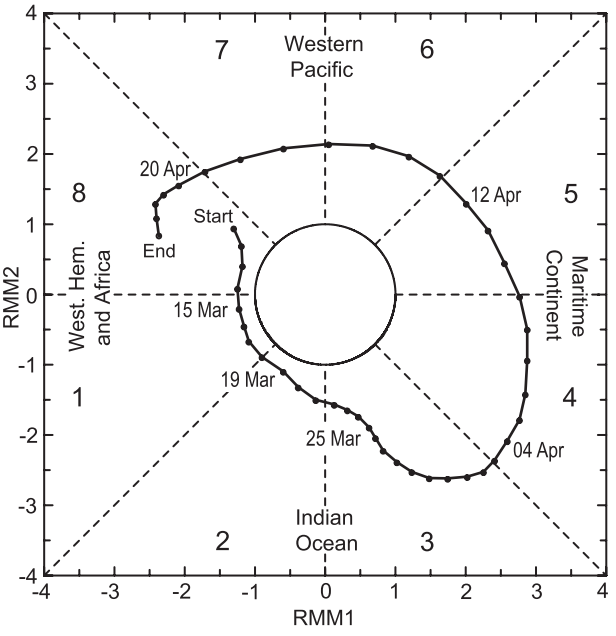

FIG. 4. The time evolution between 11 Mar and 24 Apr 2005 of the MJO in a phase-space diagram of normalized anomalies (units of standard deviation) defined using 2 ''multivariate'' empirical orthogonal functions. A 5-day running mean is applied to the daily data. The dots on the observed trajectory are 1 day apart, which grows in magnitude as it moves through phases 8–1–2–3. The timing of the baroclinic wave packets (EWPs) that dispersed into the Pacific basin from Asia are marked in the figure, as well as some selected other dates to orient the reader.

of the raw T_b fields (e.g., Wheeler et al. 2000; Wheeler and Weickmann 2001; Kiladis et al. 2009).

Figure 4 uses an MJO phase diagram (Wheeler and Hendon 2004) to illustrate the evolution of the MJO from phase 1 on 15 March 2005 to phase 3 by 25 March 2005, an 11-day period. The phase and amplitude are based on projections of daily anomalies onto 15°N–15°S averaged patterns of u at 200 hPa, u at 850 hPa, and outgoing longwave radiation (OLR) that describe the MJO. Interannual ENSO anomalies and a 120-day running mean are removed from the daily anomalies. MJO composite studies during phases 1–3 show that, on average, the Pacific upper-tropospheric circulation transitions to a pattern of stronger equatorial westerlies tied to the eastward translation of subtropical anticyclonic anomalies into the west Pacific (e.g., Knutson and Weickmann 1987). This pattern in turn favors stronger than normal extratropical wave energy dispersion into the tropical eastern Pacific (e.g., Matthews and Kiladis 1999). In this section, these large-scale circulation changes are examined for this case to provide a context for the AR. This includes the role of baroclinic disturbances coming off the Asian continent, their amplification along the coast, and the southeastward dispersion of energy into the Pacific.

Figure 5 shows the evolution of the 150-hPa streamfunction perturbation and CLAUS brightness temperature fields for two selected days leading up to the storm event in the Pacific Northwest shown in Fig. 2. The raw CLAUS T_b is shown, and the mean and first three harmonics of the mean 1997–2008 seasonal cycle have been subtracted from the streamfunction field to calculate anomalies. The T_b field in Fig. 5 has been shaded to represent regions of convection within the tropics, with colder temperatures indicative of deeper clouds.

At 0600 UTC 23 March 2005 (Fig. 5a), MJO convection has become established along the equator in the eastern Indian Ocean and is extending across Indonesia, in part due to the eastward movement of event K1 into Sumatra (as highlighted in Fig. 3). Farther north, over western Asia, a cyclone has developed around 55°N, 40°E and represents the western portion of an EWP (yellow arrow) that has alternating circulation centers extending eastward into the central Pacific. Subsequently, the Eurasian portion of the wave train weakens as the Pacific centers strengthen over time (not shown), a typical signal of southeastward energy dispersion.

By 0600 UTC 26 March (Fig. 5b), the North Pacific EWP is at its peak amplitude, after wave energy has propagated well into the eastern Pacific, thereby contributing to a well-defined positive tilt of synoptic eddies that extends toward the Pacific Northwest. The Pacific convective field is determined in part by the series of Kelvin pulses (K1–K3) that emanate to the east of the MJO convection, along with the southward portion of the trough extending into disturbance K2. In particular, the ITCZ convection that the AR taps into in Fig. 5b appears to be reinforced by K2. The AR is embedded within anomalous southwesterly flow between a positively tilted upper-level subtropical ridge to its east, and a similarly tilted trough to its west. The signature of this trough extends from the Gulf of Alaska all the way down to the equatorial region near the date line, and wave energy is seen to have propagated well into subtropical North America. From Hovmöller diagrams (not shown) the Rossby wave energy with the AR-linked event disperses at a relatively fast speed of ~40 m s^{-1}.

In summary, extratropical wave energy propagating into the tropics and interacting with ITCZ convection was shown by Matthews and Kiladis (1999) to be statistically favored when MJO convection is in the eastern Indian Ocean (MJO phases 3 and 4). On average during this time, convection is moving toward the Maritime Continent and large-scale downstream troughs are being established first over the western Pacific and then the central and eastern Pacific basin. This is a favorable base state for equatorward energy dispersion (Matthews and Kiladis 1999), since westerlies are more uniform in

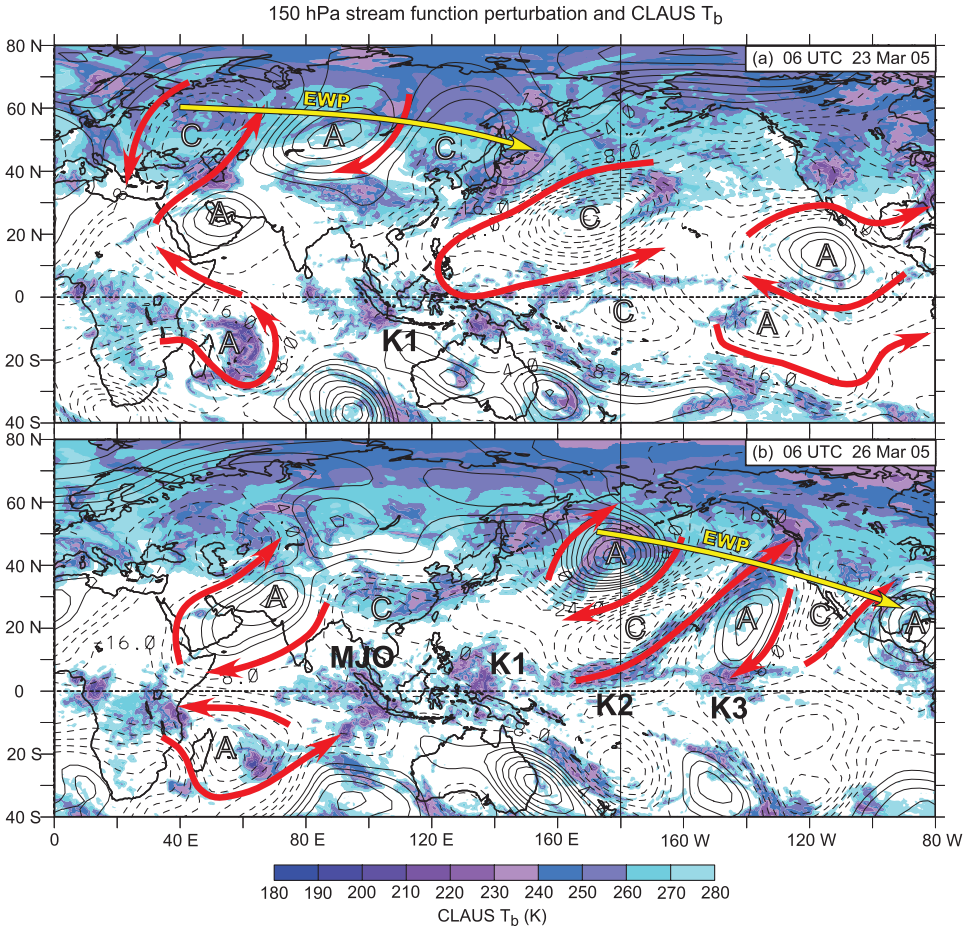

FIG. 5. The 150-hPa streamfunction anomalies (contours) and CLAUS T_b data (color scale; K) at 0600 UTC on (a) 23 and (b) 26 Mar 2005. The streamfunction anomalies are computed by removing the first three harmonics of the mean seasonal cycle from 1979 through 2008. The A and C annotations refer to anticyclonic and cyclonic circulation centers, respectively. The red arrows highlight dominant wind directions having large magnitudes (roughly proportional to the streamfunction gradient) and represent snapshots of evolving and interacting midlatitude and tropical (MJO and Kelvin wave) weather–climate systems. The streamfunction contour interval is 4×10^5 m^2 s^{-1}, with the 0 contour omitted. Yellow arrows show the mean direction of EWP energy dispersion.

latitude in the upper troposphere over the eastern Pacific Ocean. Such dispersion provides for coherent, meridionally extended, and positively tilted disturbances that are more likely to reach into the tropics and establish an elongated AR connecting the tropics to the mid- and high latitudes of western North America. While this case study shows a well-defined series of related events that set the stage on the planetary scale for the AR to tap the tropics, we reemphasize that ARs can develop through widely varying mechanisms, many of which do not necessarily involve equatorward-propagating EWPs or direct transport of tropical moisture (e.g., Bao et al. 2006). A statistical analysis of more cases is under way in order to assess the representativeness of this particular event.

4. SSM/I and aircraft observations of the atmospheric river

As discussed earlier, the sequence of SSM/I IWV images in Fig. 2 shows the eastern Pacific AR exiting the tropical water vapor reservoir southwest of the Hawaiian Islands and extending northeastward as a narrow IWV plume. During this 2-day period between 24 and 26 March 2005, the plume moved eastward across Hawaii while elongating to the U.S. Pacific Northwest. Time series traces of IWV measured by GPS receivers at KOK and FTS (Fig. 2d) show a period of enhanced water vapor content as the AR impacted each site. The amplitude of the IWV maximum (KOK, 4.32 cm at 1445 UTC 25 March; FTS, 2.84 cm at 1445 UTC 26 March) was 1.48 cm larger

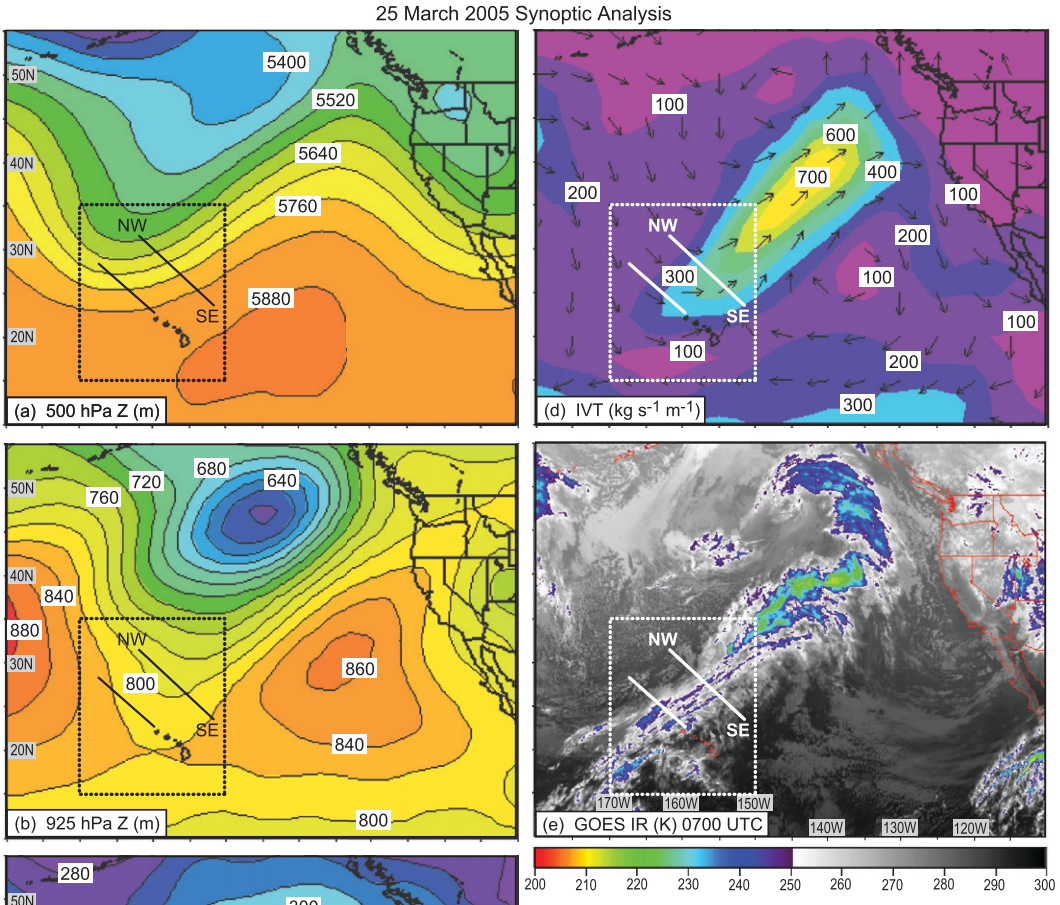

FIG. 6. Composite analyses derived from the NCEP–NCAR reanalysis dataset for 25 Mar 2005: (a) 500-hPa geopotential height (Z, m), (b) 925-hPa geopotential height (Z, m), (c) 925-hPa equivalent potential temperature (θ_e, K), and (d) vertically integrated horizontal water vapor transport (IVT, kg s^{-1} m^{-1}). (e) *GOES-10* 10.7-μm channel (IR) image of surface and/or cloud-top brightness temperature (K, color bar at bottom) at 0700 UTC 25 Mar 2005. The inset box and dropsonde curtain baselines shown in Fig. 2a are also displayed here.

at KOK owing to its proximity to the tropical water vapor reservoir, and possibly also due to rainout between there and FTS, although the enhanced IWV persisted for a longer period at FTS. Given that the AR exhibited a similar cross-plume width at both sites, the broader maximum at FTS reflected the fact that the AR moved more slowly across this site in response to a transient frontal wave in the vicinity (discussed in more detail in section 5). Details of the AR's structure within the inset box of Fig. 2a will be presented later in this section.

Daily mean fields constructed from the NCEP–NCAR global reanalysis dataset on 25 March 2005 (Figs. 6a–d) highlight the synoptic conditions over the northeastern Pacific associated with the landfalling AR, as does the GOES infrared satellite imagery (Fig. 6e). The 500-hPa geopotential height analysis (Fig. 6a) portrays a positively tilted open trough penetrating deep into the subtropics immediately west of Hawaii and a closed anticyclone just to the east of the islands. This trough–ridge couplet propagated eastward with time. A companion

geopotential height analysis at 925 hPa (Fig. 6b) shows an extratropical cyclone situated west of Vancouver Island and a trough axis extending southward to Hawaii, bifurcating the subtropical high located northeast and northwest of the islands and deflecting the trade winds and associated low-level moisture poleward into the midlatitude cyclonic circulation [cf. the equivalent potential temperature (θ_e) analysis in Fig. 6c]. The location of this θ_e plume closely matches that of the IWV plume associated with the AR in Fig. 2b, and also coincides with the axis of maximum vertically integrated horizontal water vapor transport or flux (IVT[1]) directed northeastward toward the Pacific Northwest (Fig. 6d). The IVT analysis also shows transport of water vapor northward from the tropics into the tail of the AR. The maximum value of IVT at this time exceeded 700 kg s^{-1} m^{-1}, which is stronger than the median value of 600 kg s^{-1} m^{-1} within 117 cool-season (October–March) ARs making landfall in the Pacific Northwest during the eight water years of 1998–2005 (Neiman et al. 2008b). A GOES infrared satellite image at 0700 UTC 25 March (Fig. 6e) contains a southwest–northeast-oriented band of cold cloud tops in the vicinity of the AR and trailing cold front that spiraled inward toward the extratropical cyclone center.

Figures 6 and 7 provide the large-scale context for the dropsonde cross section (Fig. 8), located near the tail of the AR in southwesterly flow aloft, within the trough at low levels, and across the θ_e plume and trailing cold front. The dropsonde curtains were spatially adjusted such that the dropsonde containing the largest IWV in each curtain was positioned over the core of the SSM/I IWV plume in Fig. 7a. Core IWV values in the AR were 3.33–4.33 cm north of Hawaii, where large CLW (>200 g m^{-2}; Fig. 7b) and significant rain rate (as large as 16 cm day^{-1}; Fig. 7c) were collocated. A secondary, less organized IWV plume and associated swath of enhanced CLW extended northeastward from the islands toward the AR although rainfall was absent.

The vertical structure across the AR and secondary IWV plume, and the differences between them, are shown in a cross section along line NW–SE in Fig. 7, based on 20 dropsondes spanning ~1350 km between 0040 and 0300 UTC 25 March (Fig. 8). Analysis of the along-front wind U and water vapor specific humidity q (Fig. 8a) clearly marks the position of the northwestward-sloping polar cold front, where strong frontal shear and a coincident moisture gradient occurred. A plume of moisture was situated in the southwesterly flow near the leading edge of the front (13 g kg^{-1} near the surface) and penetrated vertically to above 500 hPa.[2] Farther southeast, low-level moisture was even greater (>14 g kg^{-1}), but was capped by much drier air.

The U and q fields were combined into an analysis of horizontal along-front water vapor flux from the surface to 500 hPa (Fig. 8b) using the technique described in Ralph et al. (2004). The flux analysis shows the AR situated on the warm side of the cold front. The AR penetrated vertically to at least 500 hPa and sloped up the warm side of the front. Flux values peaked on the warm side of the front at ~800 hPa (>100×10^5 kg s^{-1}), while the front itself marks a zone of strong flux gradient. This low-latitude AR is similar in structure and magnitude to one observed with dropsondes several years earlier in the midlatitudes offshore of California (Ralph et al. 2004). The flux analysis in Fig. 8b resulted from slightly weaker low-level winds embedded in moister conditions than that observed in its midlatitude counterpart. Southeast of the AR, strong fluxes were confined to the lower troposphere in the region of shallow moisture (see Fig. 8a).

A companion cross-section analysis of θ_e (Fig. 8c) depicts a well-defined θ_e gradient with the cold front, and a vertically oriented θ_e plume exceeding 328 K within the AR. The upright character of the plume originating at the leading edge of the front at the ocean surface is strongly suggestive of frontally forced deep convection. In fact, the P-3 recorded in-flight convective perturbations at 425 hPa over the θ_e plume, and airborne radar observed convective elements in this region (not shown). Also, the SSM/I overpass at 1744 UTC 24 March (Fig. 7c) recorded a narrow band of precipitation in the AR, further evidence that deep convection was triggered by the cold front. In the southeast half of the cross section, low-level θ_e exceeded 332 K, above which a layer of significant potential instability ($-\partial\theta_e/\partial p < 0$) separated the moist low levels from much drier air aloft. However, given that convective inhibition was too great to overcome in this region lacking mesoscale triggering mechanisms (not shown), convection was not observed.

Figure 8d shows a dropsonde depiction of the IWV and companion along-front vertically integrated horizontal water vapor flux. The dropsonde IWV trace captures the double water-vapor peak shown in Fig. 7a, the larger of which is tied to the AR. The flux trace mirrors its IWV counterpart, except in the region of the secondary IWV peak. This disparity arises because the very moist lower troposphere here is accompanied by weaker flow than

[1] IVT is calculated from the surface to 300 hPa [see Neiman et al. (2008b) for a description of the methodology].

[2] A second cross section, positioned southwest of line NW–SE in Figs. 6 and 7, is qualitatively similar in its depiction of the cold frontal region but will not be shown for the sake of brevity.

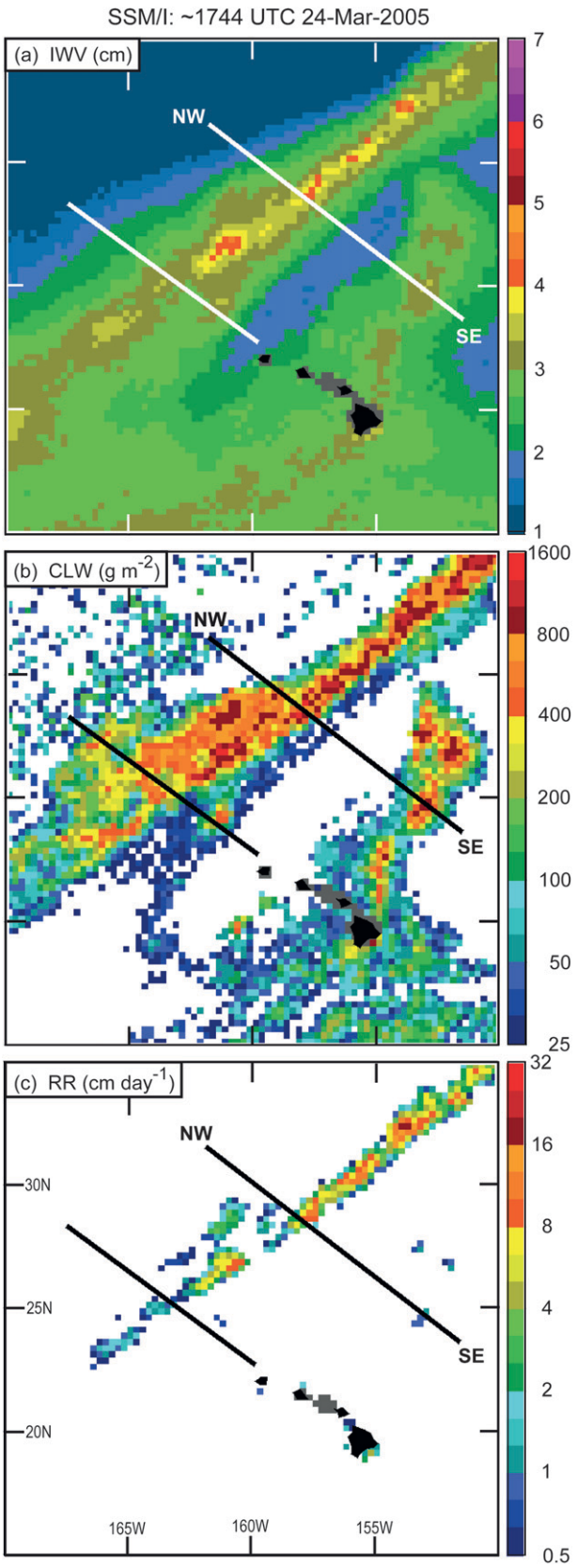

that found in the AR, and because the flow aloft in this region is weaker and much drier than in the AR. Hence, despite the fact that the SSM/I IWV and CLW images (Figs. 7a and 7b) showed reasonably similar values in the AR and in the secondary plume farther southeast, the dropsondes revealed markedly different vertical structures in these two regions. The sequence of SSM/I IWV images in Fig. 2 suggests that this secondary IWV plume was incorporated into the overall AR farther northeast over the next 2 days, although no direct observations are available to confirm this.

5. Hydrometeorological impacts in the Pacific Northwest

The offshore observations and analyses highlighted above were made within the developing AR 1–2 days prior to its landfall in the Pacific Northwest. In this section, hydrometeorological impacts during landfall in northwestern Oregon are examined using the land-based instrumentation described in section 2 (see also Fig. 9).

A time–height section of hourly wind profiles and along-front isotachs at AST (Fig. 10a) shows the temporal descent of enhanced shear associated with a warm front between ~1 km MSL at 0400 UTC 26 March 2005 and the surface at 1215 UTC 26 March 2005, followed by a >32 m s^{-1} southwesterly LLJ centered at 1 km MSL and strong southwesterly surface flow (Fig. 10b) in the core of the AR. This is comparable to the LLJ magnitudes documented in Ralph et al. (2006) that were associated with seven flooding events on the Russian River. During the warm-frontal descent and within the warm sector, parallel axes of geostrophic warm advection were observed [based on the geostrophic thermal advection diagnostic in Neiman and Shapiro (1989)], resulting in incremental rises in the altitude of the brightband melting level. Additional surface traces (Fig. 10b) reveal a rapid ~8-K increase in θ_e, a steady decrease in pressure, and enhanced rainfall with the descent of the warm front. Companion GPS observations at nearby FTS (Fig. 10c) documented a steady increase in IWV beyond the 2-cm minimum AR threshold (Ralph et al. 2004) during the warm-frontal descent, and values exceeding 2.8 cm within the AR warm sector. This value of IWV matches the

←

FIG. 7. SSM/I satellite imagery centered at ~1744 UTC 24 Mar 2005 of (a) IWV (cm), (b) CLW (g m^{-2}), and (c) rain rate (RR; cm day^{-1}). The solid lines portray the time-to-space-adjusted NOAA P-3 dropsonde transects (as in Figs. 2a and 6). The line labeled NW–SE is the projection line for the cross section in Fig. 8.

mode of the distribution of 117 ARs that struck the Pacific Northwest from 1997 to 2005 (Neiman et al. 2008b). The along-front bulk IWV flux[3] behaved similarly, approaching 100 m s^{-1} × cm in the AR where water vapor transports are strongest (e.g., see also Fig. 8). This magnitude of bulk water vapor flux is in the top 10% of values documented in events over four winters in California (Neiman et al. 2009).

Starting at ~1600 UTC 26 March, a descending zone of cooling above the LLJ was inferred by the AST profiler at ~3 km MSL, as evidenced by the commencement and subsequent descent of geostrophic cold advection, a descending melting level, and a modest decrease in surface wind speed and IWV. Seven hours later (i.e., near 2300 UTC), a robust, surface-based cold front accompanied by a 1.5-km-deep wind shift from strong southwesterly to weak westerly flow crossed the profiler. From 2000 to 2300 UTC 26 March 2005, precipitation increased in intensity with the approach of the front during a period of inferred static destabilization (i.e., warm advection beneath cold advection) below 3 km MSL. The IWV flux decreased sharply and the surface pressure increased by 1.3 mb with the cold-frontal passage, marking the end of the initial phase of the AR landfall at AST. Moderate and prolonged rain fell in the coastal mountains during this initial phase (Fig. 10d), with a corresponding increase in runoff in the Nehalem River starting at 0300 UTC 26 March (Fig. 11). Following the cold-frontal passage, the flow remained comparatively weak through a deep layer between 2330 UTC 26 March and 0415 UTC 27 March, during which time the melting-level altitude, the IWV, and the IWV flux were suppressed, and the rainfall at AST slackened. Above ~3.5 km, a temporally ascending zone of geostrophic cold advection between 2200 UTC 26 March and 0200 UTC 27 March marked the temporary downward extension of the upper-tropospheric polar jet-front system.

Strong warm-frontal shear and geostrophic warm advection returned to AST aloft at ~0400 UTC 27 March and quickly descended to the surface by 0800 UTC, during which period the melting level rose modestly, the IWV increased steadily, the IWV flux strengthened markedly, and the heaviest rain of the event fell at AST. The surface θ_e jumped abruptly ~4 K with the frontal passage, followed by a >28 m s^{-1} southwesterly LLJ at ~1 km MSL and strong southwesterly flow at the surface. The IWV flux attained a peak value exceeding 70 m s^{-1} × cm within this secondary warm sector, thus signifying the return of AR conditions. At 1000 UTC, a new zone of temporally descending geostrophic cold advection commenced at 3 km MSL. The forward-tilted cold front reached the surface at 1330 UTC and was characterized by a sharp wind shift from strong southwesterly to weak northwesterly coinciding with a rapid 5-K decrease in surface θ_e. During the cold-frontal descent, the melting level dropped, the IWV decreased to below the 2-cm minimum AR threshold, and the IWV flux abated abruptly. A brief period of light rainfall accompanied the surface frontal passage. Geostrophic cold advection with the upper-level jet-front system reappeared above 3.8 km after 0900 UTC 27 March.

The wind profiler isotach and IWV flux analysis in Fig. 10 provide unambiguous documentation of a transient frontal wave impacting northwestern Oregon between 0400 and 1400 UTC 27 March, during which period the surface pressure dropped 11 mb before partially recovering. This wave is clearly tracked in the IR satellite imagery across the eastern Pacific (Fig. 12) as an amplifying baroclinic cloud leaf along the polar cold front (see Fig. 15c for isochrones of the frontal wave corresponding to this cloud leaf). While this frontal wave represents a deformation of the primary cold front, it does not appear to have generated a secondary cyclone. An earlier example of such a frontal wave was documented by Neiman et al. (2004) using research aircraft, wind profilers, and Next Generation Weather Radar (NEXRAD) radar. Additional annotation in the imagery provides mesoscale context at AST based on the wind-profiler analysis. As is often the case for West Coast storms, the relative sparseness of surface observations offshore and of NEXRAD radar coverage precludes detection of frontal waves of the scale present in this case. It is one of the unique capabilities of coastal wind-profiling technology, especially when combined with surface meteorology and GPS IWV data, that these waves can become apparent. However, their signatures are found most readily in time–height cross sections, such as Fig. 10 and in Neiman et al. (2004), rather than in traditional plan-view maps.

In the nearby coastal mountains at SFK (Fig. 10d), the heaviest rain of the AR event fell during the frontal wave. Total rainfall for the entire AR event approached 200 mm, roughly 4 times that observed along the coast at AST. Orographic processes enhanced the rainfall in the mountains due to strong low-level vapor fluxes, reduced static stability, and greater water vapor content in the AR environment (e.g., Neiman et al. 2002; Ralph et al. 2005a; Neiman et al. 2008b, 2009). As shown by Persson

[3] The along-front bulk IWV flux is defined as the product of the along-front component of the flow measured hourly by the AST wind profiler in the layer between 750 and 1250 m MSL and the hourly IWV measured at the nearby GPS receiver at FTS. A variant of this technique is described in Neiman et al. (2009). Because water vapor is typically concentrated in the lower troposphere, the IWV flux is a first-order estimate of low-level water vapor flux.

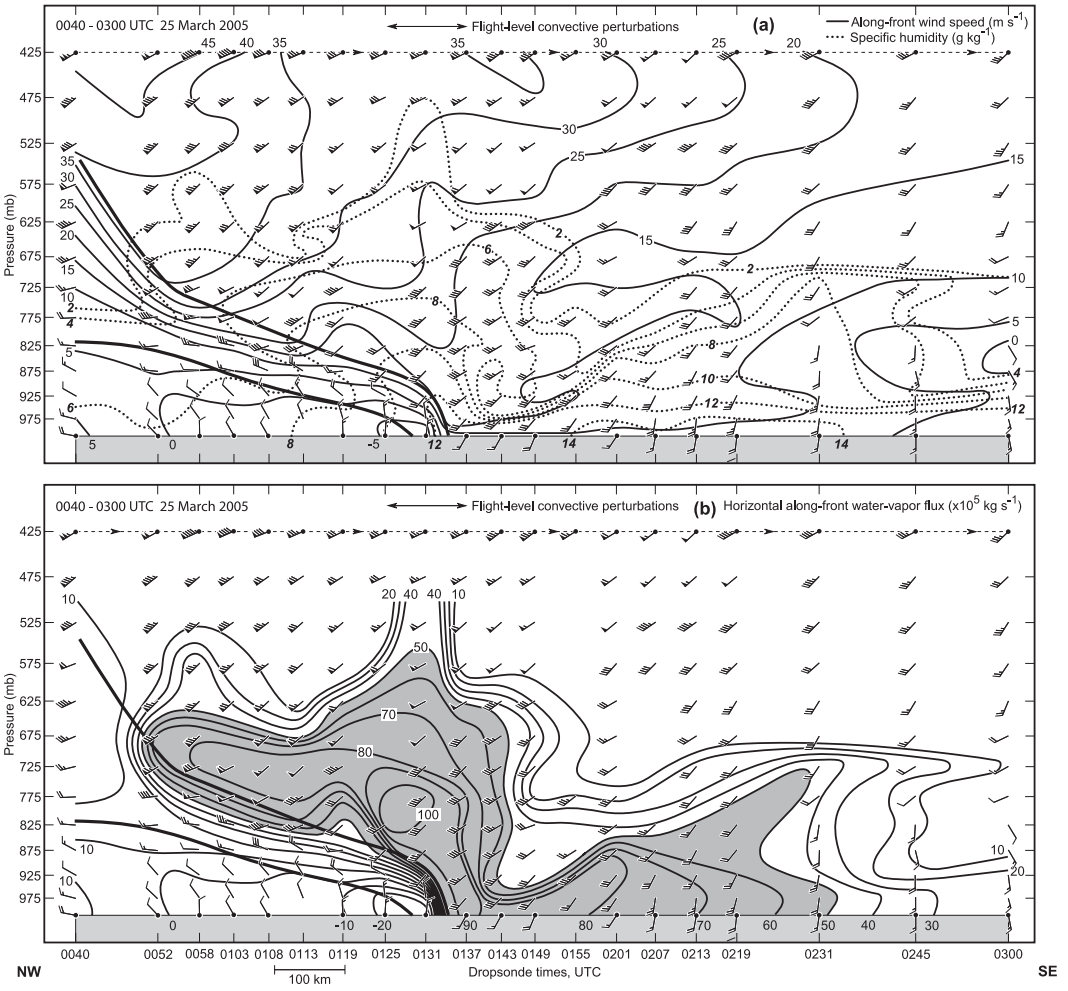

FIG. 8. NOAA P-3 cross sections along line NW–SE in Fig. 7 valid at 0040–0300 UTC 25 Mar 2005: (a) along-front wind speed (m s^{-1}, directed from 230°, solid) and water vapor specific humidity (g kg^{-1}, dotted), (b) horizontal along-front water vapor flux ($\times 10^5$ kg s^{-1}; shading, $>50 \times 10^5$ kg s^{-1}), and (c) equivalent potential temperature (K; dark shading, >328 K; light shading, < 316 K). Wind flags = 25 m s^{-1}, barbs = 5 m s^{-1}, and half-barbs = 2.5 m s^{-1}. The thin dashed line at ~425 hPa portrays the NOAA P-3 flight track. Frontal boundaries are marked with boldface black lines. (d) Time series of integrated water vapor (cm, dashed) and vertically integrated horizontal along-front water vapor transport ($\times 10^5$ kg s^{-1}, solid) from the dropsondes. The times (UTC) of dropsonde deployments on 25 Mar 2005 are given.

et al. (2005), these conditions can lead to greater convective available potential energy. The frontal wave retained moist AR conditions [e.g., IWV >2 cm, a threshold identified by Ralph et al. (2004)] and resultant heavy rainfall in northwestern Oregon for at least ~34 h. Farther southeast at SLE, the frontal wave remained north of the area, thus prolonging deeper AR moisture at that site for nine additional hours (Fig. 10c).

To better define the relationship between the duration of AR conditions and the passage of the frontal wave, a simple graphical method was developed to allow a mapping of the duration of AR conditions over the region. This approach follows logic laid out by Doswell et al. (1996) whereby the combination of the shape and movement of a heavy rain producing region can be combined to identify specific areas that would be exposed to heavy rainfall for the longest period. In the analysis used here, the feature that produces the heavy rainfall is interpreted to be the region of AR conditions, which resides adjacent to and on the warm side of the surface front, and is on average roughly 400 km wide. While this would normally produce a spatial pattern of ''AR duration'' that is uniform across the region, the presence of the frontal wave modifies this pattern substantially due to the combined effects of the along-front propagation of the frontal wave, with the overall movement of the

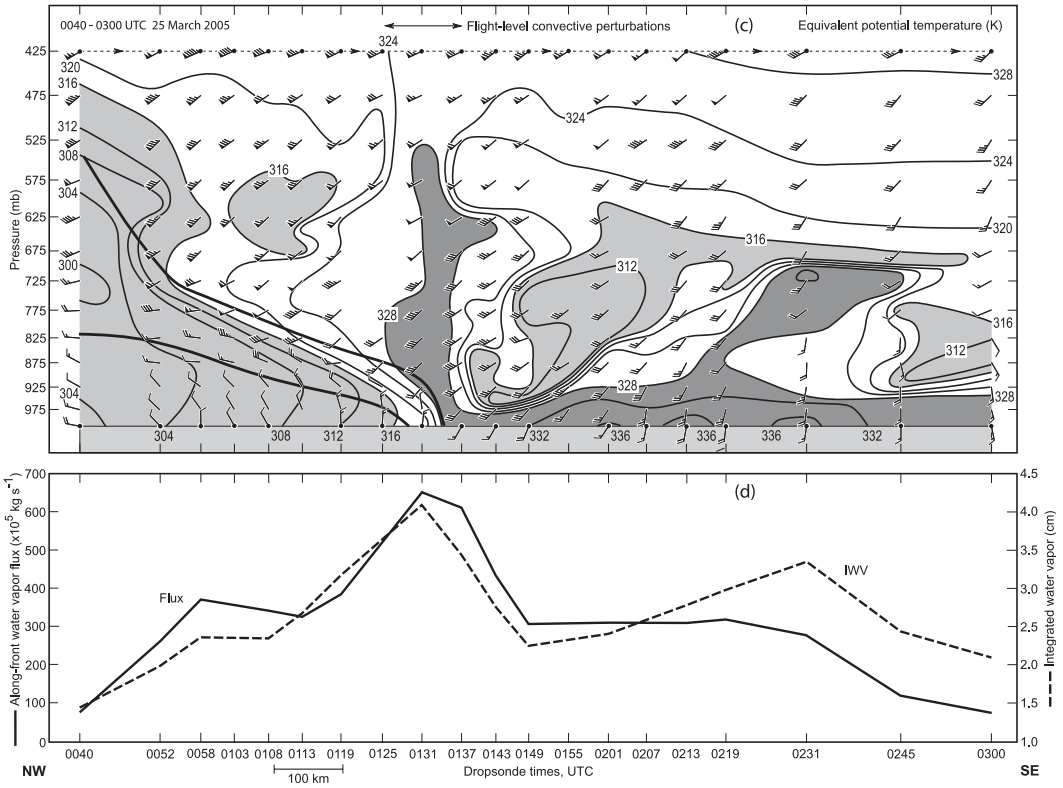

FIG. 8. (*Continued*)

larger-scale frontal system (with its associated AR). The method developed here used the width of the AR derived from SSM/I estimates, plus an isochrone analysis derived from the satellite imagery in Fig. 12, where the isochrone movement represents a combination of both the frontal wave propagation and the movement of the synoptic-scale trough. Assuming that the frontal wave created a horizontal displacement of the AR relative to its position without the frontal wave (as supported by the profiler analysis), the propagation of the AR across the region was estimated graphically over the 1.5-day period from 0700 UTC 26 March to 1830 UTC 27 March 2005. From this, a plan-view contour analysis was derived of the duration of AR conditions in the region off the Pacific Northwest coast (e.g., see Fig. 15c described in section 7a). The graphical method yielded an estimate of a maximum duration of 28–30 h, centered over the area that experienced the heaviest precipitation. Independent analysis presented earlier from the profiler, GPS-met, and precipitation data estimated maximum duration of 34 h, suggesting the simple graphical method was reliable in this case. The conclusion that a mesoscale region was exposed to AR conditions and heavy orographic precipitation created substantial runoff is consistent with conclusions by Doswell et al. (1996) that the duration of moderate or heavy precipitation amplifies the flash flood threat.

The landfalling AR and associated transient frontal wave, which occurred during a period of drought, yielded

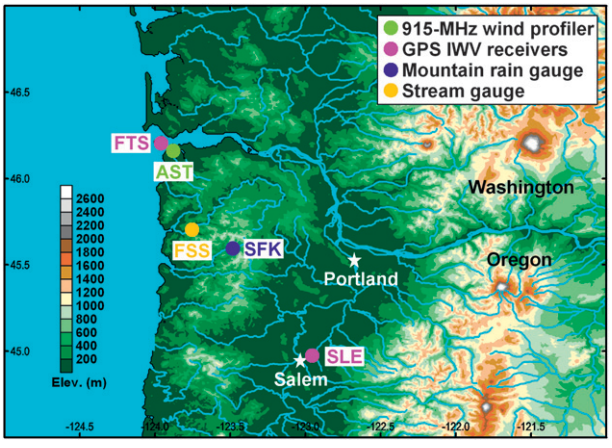

FIG. 9. Terrain base map of northwestern OR and southwestern WA. The following key observing sites are marked: AST = 915-MHz wind profiler at Astoria; FTS and SLE = GPS receivers at Fort Stevens and Salem, respectively; SFK = rain gauge at South Fork; and FSS = stream gauge at Foss.

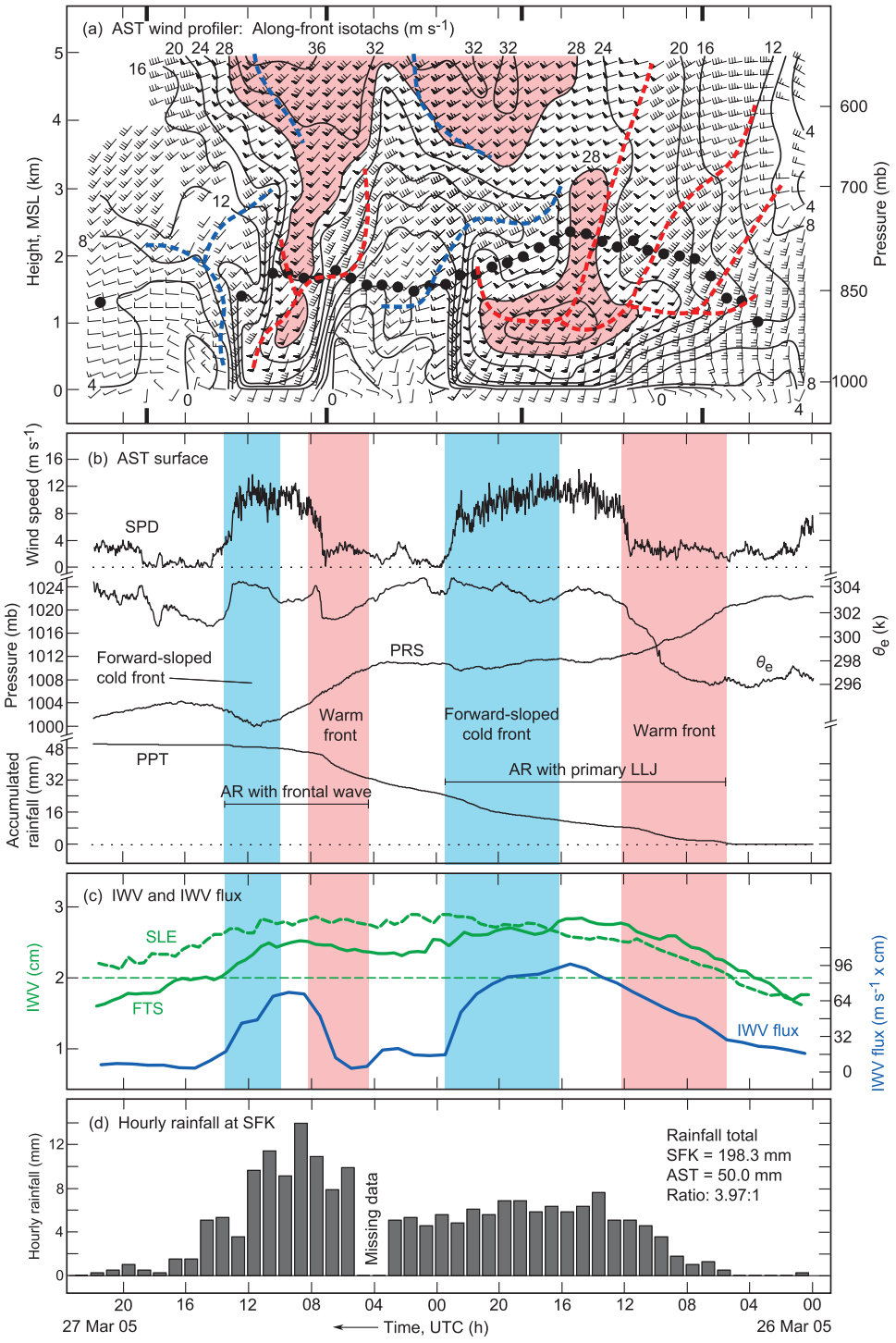

FIG. 10. Time series of observations from northwestern OR between 0000 UTC 26 Mar and 22 UTC 27 Mar 2005. Time increases from right to left to portray the advection of fronts from west to east. (a) Time–height section of hourly averaged wind profiles (flags and barbs are as in Fig. 8), along-front isotachs (m s^{-1}, directed from 220°; >28 m s^{-1} red shaded), brightband melting-level heights (bold black dots), and axes of maximum thermal wind-derived (i.e., geostrophic) warm and cold advection [red and blue dashed lines, respectively; derivation technique described in Neiman and Shapiro (1989)] from the AST wind profiler. Every other range gate is plotted. Boldface tick marks correspond to the times of the IR satellite images in Fig. 12. (b) Time series of surface data from the AST wind profiler [SPD, wind speed

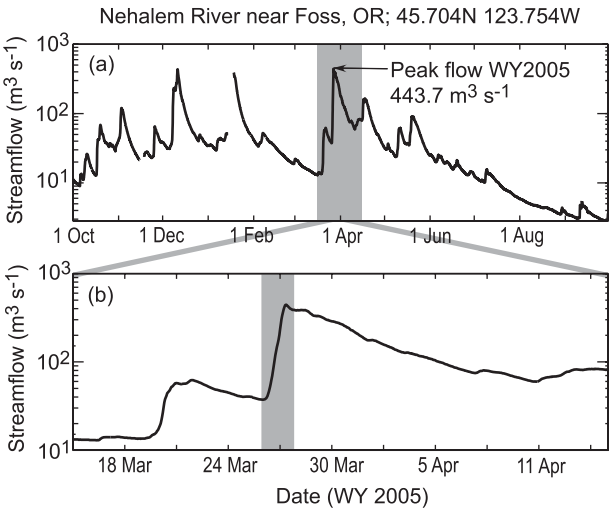

FIG. 11. Hydrographs ($m^3\ s^{-1}$) from the Nehalem River stream gauge near Foss for (a) water year 2005 and (b) 15 Mar–15 Apr 2005. The gray-shaded bar in (a) marks the time window of (b), and the gray-shaded bar in (b) marks the span of the time series in Fig. 10.

a peak streamflow at FSS of ~444 $m^3\ s^{-1}$ at 0800 UTC 27 March (Fig. 11), just surpassing flood monitor stage. This was the largest recorded flow at this gauge during water year 2005. The two other large peaks, on 10–12 December 2004 and 18–19 January 2005, also occurred during ARs, and the December AR appeared to also tap tropical Pacific moisture.

6. Discussion of forecast uncertainty for the case studied here

This section illustrates key challenges of forecasting conditions associated with this AR and extreme precipitation. The Global Forecast System (GFS) ensemble-based estimates of forecast uncertainty are shown in Fig. 13 using 500-hPa height and methods developed by Toth et al. (2005) to quantify this uncertainty. Three lead times relative to the date of heaviest precipitation (0000 UTC 27 March 2005) are used to demonstrate the model's ability to capture important aspects of the large-scale flow at 500 hPa. Precipitation data were not available for the forecasts beyond 3-day lead time.

Comparing Fig. 13a with Figs. 13b and 13c shows a synoptic-scale ridge–trough geopotential height pattern west of 140°W that is better predicted at 4- than at 7-day lead time, at least relative to the best forecast shown (1-day lead time; see Fig. 13c). Note in particular the more prominent NE–SW tilt of the ridge–trough, its shorter zonal scale, and the low heights over western Alaska for the 24-h forecast. Initial conditions on and after 23 March (e.g., see Fig. 5b) captured these important features of the large-scale circulation. This is supported by the high degree of probability of verification of the ridge seen in the red shading around the date line and 30°N in Figs. 13b and 13c. However, east of the ridge, a low degree of probability of verification is evident with the downstream trough especially in the strong southwesterly flow. This is relative to other 24-h forecasts in the last 30–40 days (Figs. 13b and 13c). In summary, while key aspects of the synoptic-scale conditions became better predicted by 4-day lead time, forecast uncertainty remained large specifically in the region containing the AR. Similarly, enhanced uncertainty in regions containing an AR was observed by Harr et al. (2008) during a period when western Pacific typhoons recurved into the midlatitude westerlies and became extratropical.

To further highlight the forecast uncertainty, and to relate it more directly to the AR, the vertically integrated horizontal water vapor flux along a direction from 220° was calculated for a 112.5-hPa-thick layer centered at 850 hPa. The values were from the GFS ensemble mean for two positions off the Oregon coast (45°N, 130°W and 45°N, 125°W) for forecasts valid at 0000 UTC 27 March 2005 as a function of lead time out to 15 days (Fig. 14). This flux varied from 0.5–2.5 units as a function of lead time before converging to 2.5 units at 125°W and 0.8 at 130°W. The largest predicted values for the position farther offshore (Fig. 14a) occurred at 5–7-day lead time, indicating the model was predicting a plume at this location that ultimately proved too far west or too broad (see verification at day 0). Closer to the coast (Fig. 14b) the predicted fluxes were relatively small at those lead times

←

($m\ s^{-1}$); θ_e, equivalent potential temperature (K); PRS, pressure (mb); PPT, accumulated rainfall (mm)]. Prominent warm- and cold-frontal periods are marked with red- and blue-shaded bars, respectively. (c) Time series of 30-min IWV (cm) from the GPS receivers at FTS (green solid) and SLE (green dashed), and time series of hourly averaged along-front IWV flux ($m\ s^{-1}$ cm; blue) centered at 1 km MSL from AST and FTS. Red and blue bars are the same as above. (d) Bar chart of hourly rainfall (mm) at SFK, together with rainfall totals at SFK and AST.

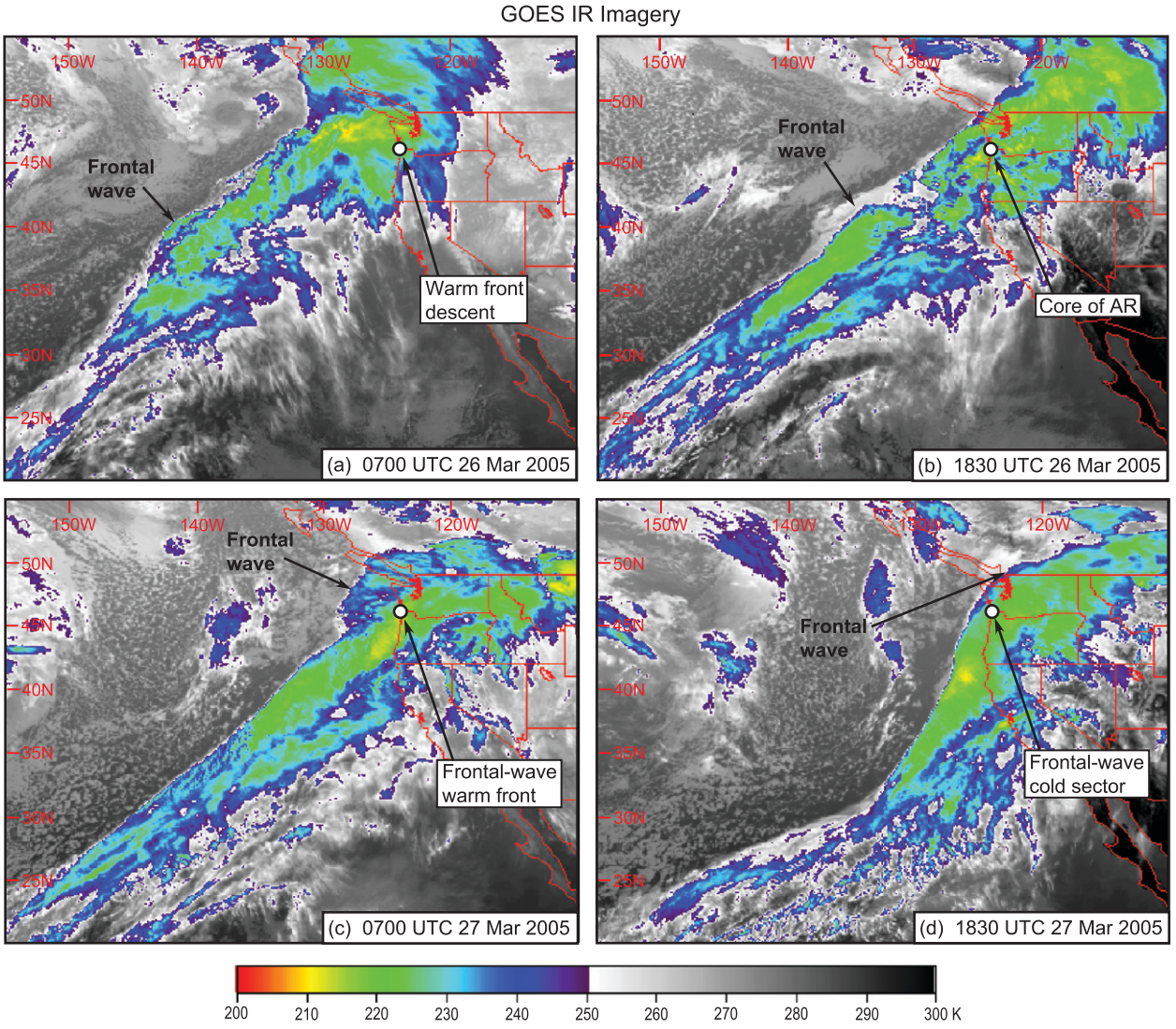

FIG. 12. *GOES-10* 10.7-μm channel (IR) images of surface and/or cloud-top brightness temperature (K, color bar at bottom) at (a) 0700 UTC 26 Mar, (b) 1830 UTC 26 Mar, (c) 0700 UTC 27 Mar, and (d) 1830 UTC 27 Mar 2005. The boldface white dot in each panel marks the location of the wind profiler at AST. Annotations are provided for this site, based on the wind profiler analysis in Fig. 10. A prominent, long-lived mesoscale frontal wave is marked in each panel.

(i.e., 5–7-day lead time) but started increasing by day 5 and reached close to their final value by day 4. This trend toward better forecasts of vapor flux at 4-day lead time closer to the coast (Fig. 14b) reflects the improvements seen in the 500-hPa height field forecasts described earlier. For shorter lead times the predicted fluxes farther offshore decreased significantly at 4- and again at 2-day lead time, overall dropping by more than 60% from 5-day lead time to verification time. For the position closer to the coast, the vapor flux only changed by 20% from day 4 to day 1 lead.

Inspection of QPF and quantitative precipitation estimation (QPE) for this event (not shown), out to 3-day lead times, showed that major precipitation was predicted in the region, but that mesoscale details were missed. Maximum precipitation in the coast range of Oregon and southern Washington, as well as Washington's Olympic Mountains, was underpredicted (150–200 mm observed versus 100–125 mm predicted), while the precipitation in coastal southern Oregon was significantly overpredicted (2.5–25 mm observed versus 50–75 mm predicted). While other factors were likely also involved, this is consistent with misplacement of the AR in the forecast, and underestimation of its strength.

This analysis highlights the challenge of predicting the large-scale and mesoscale conditions in this event,

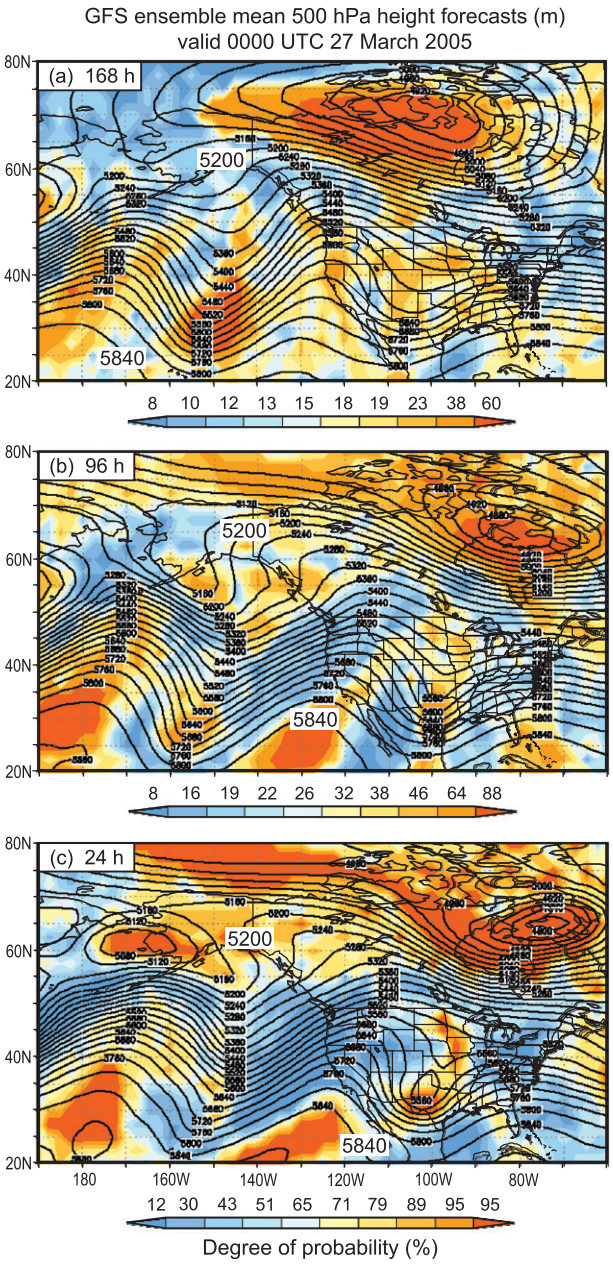

FIG. 13. GFS ensemble mean forecasts of 500-hPa geopotential heights (40-m contour interval) valid at 0000 UTC 27 Mar 2005, based on the following forecast leads: (a) 168, (b) 96, and (c) 24 h. The colors denote the degree of probability of verification (see Toth et al. 2005 for more details).

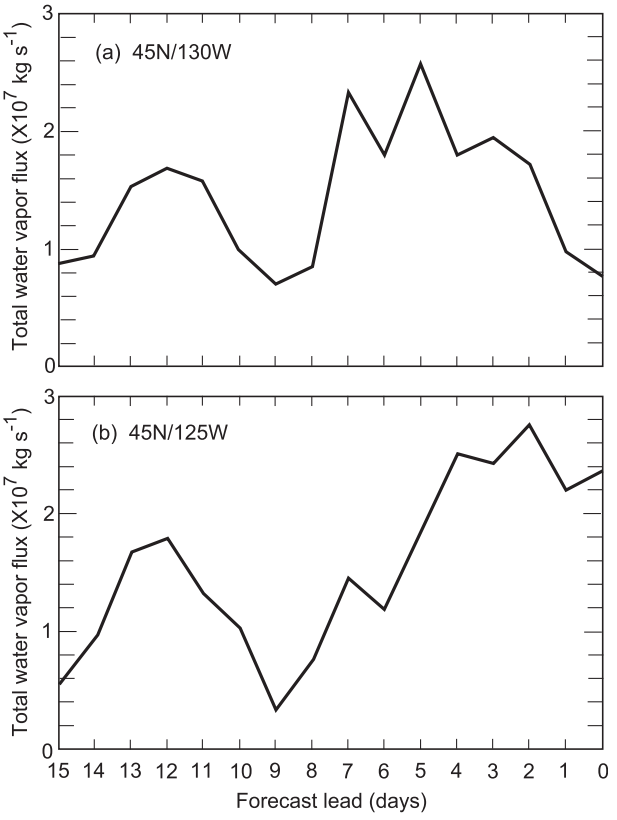

FIG. 14. Daily 850-hPa total water vapor flux ensemble mean forecasts ($\times 10^7$ kg s^{-1}, directed from 220°) valid at 0000 UTC 27 Mar 2005 from the NCEP GFS operational numerical model in 2.5° × 2.5° boxes centered at (a) 45°N, 130°W and (b) 45°N, 125°W. The depth of the boxes is 112.5 hPa centered at 850 hPa. The locations are west of the OR coast and data are shown as a function of forecast lead time out to 15 days.

including the detailed position of the AR. Ultimately to achieve accurate forecasts of the location and intensity of extreme precipitation (on scales required for accurate flood predictions), it is crucial to predict the AR's amplitude, position, and duration over a region.

7. Conclusions

a. Summary of key planetary-, synoptic-, and mesoscale factors diagnosed in this case study

This paper documented conditions in a strong AR that produced heavy precipitation on the coastal mountains of the U.S. Pacific Northwest. Although it is a single case study, it is likely that several key elements are found in many other cool-season extreme precipitation events on the U.S. west coast. These elements are described from the planetary scale to the mesoscale, partly through the use of unique experimental measurements from aircraft, wind profilers, and GPS-met. A key finding from the observations and diagnostics is that there was a direct advection of water vapor from the tropics into the southern portions of the AR in a case that later impacted the West Coast. For convenience the term tropical tap is used here and in Fig. 15, and specifically refers to the entrainment of water vapor from the band of very large IWV

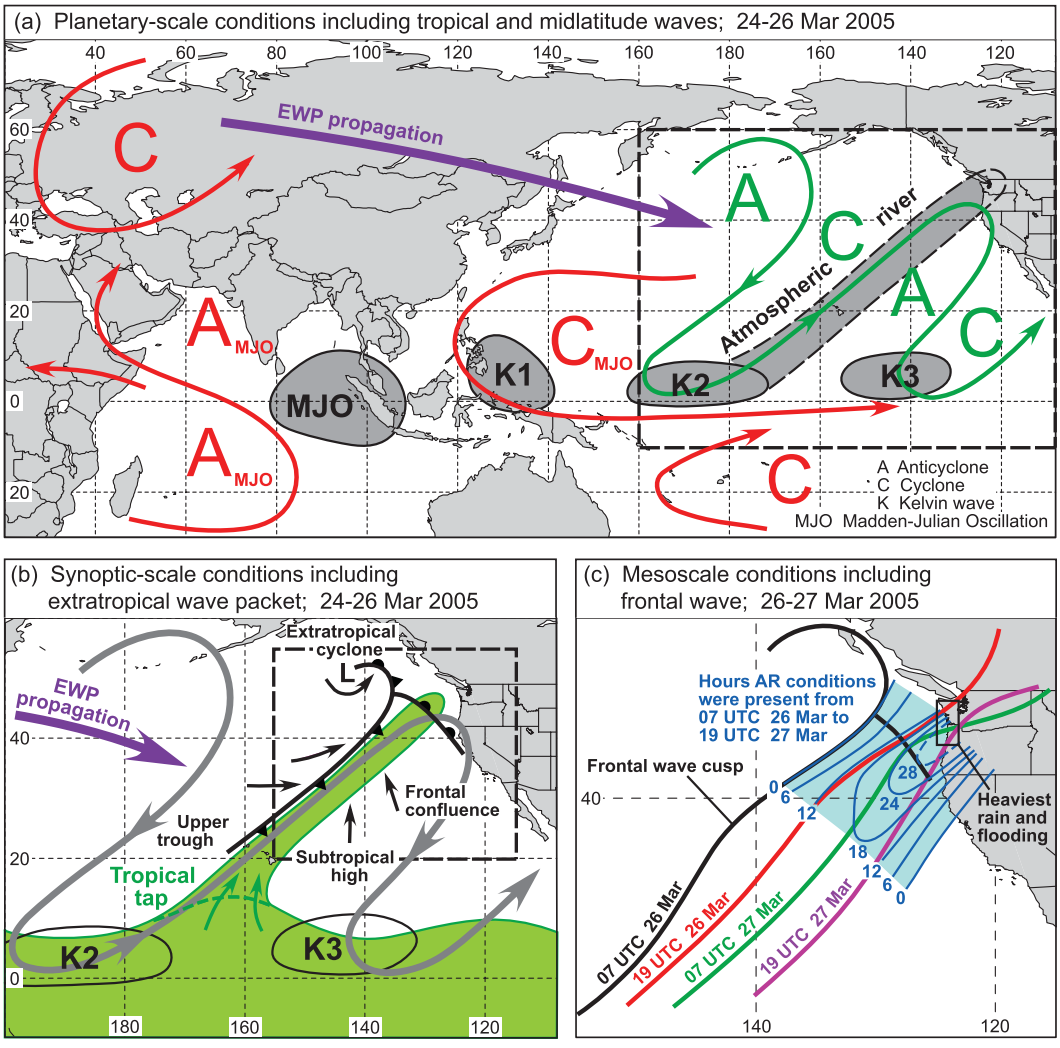

FIG. 15. Conceptual schematic for this case study depicting tropical–extratropical interactions leading to the extrusion of tropical moisture into an AR over the eastern Pacific on 24–26 Mar 2005. (a) Large-scale depiction of 150-hPa streamline anomalies (red, planetary-scale circulations; green, EWP tied to the AR). The A and C labels refer to anticyclonic and cyclonic circulation centers, respectively. The purple arrow shows the mean direction of EWP energy dispersion. Gray shading depicts CLAUS observations of coherent cold cloud tops associated with the MJO, three Kelvin waves (K1–K3), and the AR (enclosed within a dashed line). (b) Regional-scale depiction of the EWP (thick gray-shaded arrow; purple arrow shows propagation direction) and associated extratropical cyclone (standard frontal notation). Green shading depicts the tropical IWV reservoir and narrow IWV plume associated with the AR, and the green arrows depict the tapping of tropical water vapor into the AR. Kelvin waves 2 and 3 are enclosed with thin, black lines. The lower-tropospheric flow pattern is shown with black arrows. Dashed inset boxes in (a) and (b) correspond to the domains in the follow-on panels. A frontal isochrone analysis for 26–27 Mar 2005 is shown in (c), with a frontal wave propagating across the eastern Pacific and making landfall in northwestern OR where heavy rain and flooding occurred. The blue isopleths represent the number of hours of AR conditions, based on the isochrone analysis, and an assumption that the AR was 500 km wide.

found along the tropics, into the subtropical extension of the warm sector of a midlatitide extratropical cyclone, and its incorporation into an AR that then transports at least some of that water vapor into the midlatitudes. Although this advection was observed in the subtropics in this case, it should be recognized that rainout could remove much of this tropical water vapor before reaching the coast. However, trajectory studies by Bao et al. (2006) and Stohl et al. (2008) showed that tropical water vapor did contribute to precipitation in midlatitudes in at least those cases. Also, Ralph et al. (2004) used satellite data to show that rainout is relatively small on average in the subtropical extensions of ARs (see Table 5 and Fig. 23 of Ralph et al. 2004), which is consistent with the tendency for subsidence

aloft in this region. Although it is not proven in this paper, it is plausible that some of the tropical water vapor advected northward from the tropics into the AR did contribute to the heavy precipitation in Oregon in this case.

This study identifies several key physical processes that came together to create this heavy precipitation event, some of which were highlighted in a very brief earlier case shown by Doswell et al. (1996) that hit Alaska. While a number of these elements have been the focus of attention by forecasters and researchers, this study brings them together in a uniquely detailed manner, with special attention given to the role of a strong AR. The following processes played key roles in creating the heavy precipitation event, and are summarized schematically in Fig. 15:

- An MJO convective signal first formed over the tropical Indian Ocean, triggering changes in the extratropical flow concurrent with several eastward-propagating Kelvin waves in the tropics (Fig. 15a). In the extratropics a wave packet (EWP) propagated from western Asia to the Pacific where it was manifested as a wave train of amplified ridges and troughs in the eastern Pacific (Fig. 15a). Previous statistical studies show such EWPs are able to penetrate toward the equator because the MJO-modified zonal flow pattern makes the region favorable for Rossby wave propagation.
- The EWP included an extratropical cyclone in the Gulf of Alaska, with an associated cold front and well-defined atmospheric river to its south. The deep penetration into the tropics by the EWP allowed the southern portion of the extratropical trough and associated AR to reach low latitudes in the vicinity of Hawaii. The NOAA P-3 aircraft data confirmed the presence of strong northward water vapor transport in the lower troposphere deep into the subtropics (22°–32°N) near Hawaii.
- The presence of a Kelvin wave near this region had displaced the northern edge of the tropical water vapor reservoir northward. The Kelvin wave and southern portion of the AR then coincided so as to allow tropical water vapor to become entrained into the AR, forming a "tropical tap" (Fig. 15b). Because the Kelvin wave and EWP are presumed to be independent of one another, the phasing that occurred between the AR and Kelvin wave represents either a stochastic process or a fast variation favored during the 1 to 3 phase transition of the MJO. While the precise amount of tropical water vapor that was advected all the way to the U.S. west coast remains unclear, and thus its contribution to the extreme precipitation, it is plausible that this was substantial based on trajectory analysis from other case studies (e.g., Bao et al. 2006; Knippertz and Wernli 2010).
- As the AR approached the Pacific Northwest, a well-defined frontal wave developed along the primary cold front. Offshore, this was tracked using GOES IR satellite images, and was observed at the coast through analysis of detailed time–height cross sections and surface data available from the NOAA/ESRL/PSD field equipment in place. The satellite-based isochrone analysis of the frontal wave was used, along with the width of the AR to calculate the impacts of the frontal wave on the duration of AR conditions in the region (Fig. 15c). This analysis estimated a duration of slightly over 28 h in a rather limited area of the Pacific Northwest coast, which compared very well with the region of heaviest precipitation and with the independent analysis of a 34-h duration derived from the wind profiler and GPS-met observations on the Oregon coast.

b. *Future work*

From a research perspective, these results point toward the need for further, more definitive aircraft observations of the advection of tropical water vapor into ARs, as well as diagnostic studies using trajectory analysis techniques and water vapor transport budget diagnostics. The development of a meso-alpha-scale frontal wave is a crucial element of at least some extreme precipitation events along the West Coast and further research is needed to assess how best to detect and predict this important feature and changes in the AR associated with it. It is also apparent that many other physical processes can play a role in amplifying or decreasing AR strength and the precipitation they can produce upon landfall, such as air–sea fluxes from anomalously warm coastal sea surface temperatures associated with ENSO (Persson et al. 2005). Finally, the limitations of a single case study are significant, but the results from this single event lay the groundwork for extending this analysis to many other cases to help establish patterns in the key relationships. It should be noted that the month of May 2005, which followed the case studied here, was characterized by a new cycle of strong MJO activity and by the wettest May on record for portions of northern California (e.g., 236 mm in 72 h). Analysis of other similar events should yield insights regarding the importance of each element found in this case study and how those elements generate and/or modulate extreme precipitation along the U.S. west coast.

Acknowledgments. The engineering team at NOAA/PSD, led by James Jordan and Clark King, built, deployed, and maintained the land-based experimental instrumentation used in this study. Dave Kingsmill of PSD served as flight scientist during the NOAA P-3 missions. Dave Jorgensen provided algorithms and tools for flight planning. The P-3 data collection would not have been possible without Jim Churnside and coordination with his Ghostnets project conducted as part of

the same deployment. Cathy Smith of PSD developed the NCEP–NCAR reanalysis tools used in this study. Gary Wick and Darren Jackson of PSD generated the satellite imagery, Allen White of PSD created the terrain base map, and Jim Adams electronically drafted a number of the figures. This research was supported by NOAA's Hydrometeorological Testbed, NOAA's Weather-Climate Connection project, and a contract with the California Department of Water Resources.

REFERENCES

Andrews, E. D., R. C. Antweiler, P. J. Neiman, and F. M. Ralph, 2004: Influence of ENSO on flood frequency along the California coast. *J. Climate,* **17,** 337–348.

Bao, J.-W., S. A. Michelson, P. J. Neiman, F. M. Ralph, and J. M. Wilczak, 2006: Interpretation of enhanced integrated water vapor bands associated with extratropical cyclones: Their formation and connection to tropical moisture. *Mon. Wea. Rev.,* **134,** 1063–1080.

Bond, N. A., and G. A. Vecchi, 2003: The influence of the Madden–Julian oscillation on precipitation in Oregon and Washington. *Wea. Forecasting,* **18,** 600–613.

Browning, K. A., 1990: Organization of clouds and precipitation in extratropical cyclones. *Extratropical Cyclones, The Erik Palmén Memorial Volume,* C. W. Newton and E. Holopainen, Eds., Amer. Meteor. Soc., 129–153.

——, F. F. Hill, and C. W. Pardoe, 1974: Structure and mechanism of precipitation and the effect of orography in a wintertime warm sector. *Quart. J. Roy. Meteor. Soc.,* **100,** 309–330.

Carlson, T. N., 1991: *Mid-Latitude Weather Systems*. Harper-Collins, 507 pp.

Carter, D. A., K. S. Gage, W. L. Ecklund, W. M. Angevine, P. E. Johnston, A. C. Riddle, J. S. Wilson, and C. R. Williams, 1995: Developments in UHF lower tropospheric wind profiling at NOAA's Aeronomy Laboratory. *Radio Sci.,* **30,** 997–1001.

Chang, E. K. M., 1993: Downstream development of baroclinic waves as inferred from regression analysis. *J. Atmos. Sci.,* **50,** 2038–2053.

——, 2005: The impact of wave packets propagating across Asia on Pacific cyclone development. *Mon. Wea. Rev.,* **133,** 1998–2015.

Crochet, M., F. Cuq, F. M. Ralph, and S. V. Venkateswaran, 1990: Clear-air radar observations of the great October storm of 1987. *Dyn. Atmos. Oceans,* **14,** 443–461.

Dettinger, M. D., H. Hidalgo, T. Das, D. Cayan, and N. Knowles, 2009: Projections of potential flood regime changes in California: California Energy Commission Rep. CEC-500-2009-050-D, 68 pp.

Dole, R. M., 2008: Linking weather and climate. *Synoptic–Dynamic Meteorology and Weather Analysis and Forecasting, Meteor. Monogr.,* Vol. 33, Amer. Meteor. Soc., 297–348.

Doswell, C. A., III, H. E. Brooks, and R. A. Maddox, 1996: Flash flood forecasting: An ingredients-based methodology. *Wea. Forecasting,* **11,** 560–581.

Duan, J. M., and Coauthors, 1996: GPS meteorology: Direct estimation of the absolute value of precipitable water. *J. Appl. Meteor.,* **35,** 830–838.

Falvey, M., and R. Garreaud, 2007: Wintertime precipitation episodes in central Chile: Associated meteorological conditions and orographic influences. *J. Hydrometeor.,* **8,** 171–193.

Ferriday, J. G., and S. K. Avery, 1994: Passive microwave remote sensing of rainfall with SSM/I: Algorithm development and implementation. *J. Appl. Meteor.,* **33,** 1587–1596.

Harr, P. A., D. Anwender, and S. C. Jones, 2008: Predictability associated with the downstream impacts of the extratropical transition of tropical cyclones: Methodology and a case study. *Mon. Wea. Rev.,* **136,** 3205–3225.

Hodges, K. I., D. W. Chappell, G. J. Robinson, and G. Yang, 2000: An improved algorithm for generating global window brightness temperatures from multiple satellite infrared imagery. *J. Atmos. Oceanic Technol.,* **17,** 1296–1312.

Hollinger, J. P., J. L. Peirce, and G. A. Poe, 1990: SSM/I instrument evaluation. *IEEE Trans. Geosci. Remote Sens.,* **28,** 781–790.

Jankov, I., P. J. Schultz, C. J. Anderson, and S. E. Koch, 2007: The impact of different physical parameterizations and their interactions on cold-season QPF in the American River basin. *J. Hydrometeor.,* **8,** 1141–1151.

Jones, C., 2000: Occurrence of extreme precipitation events in California and the relationships with the Madden–Julian oscillation. *J. Climate,* **13,** 3576–3587.

Junker, N. W., R. H. Grumm, R. Hart, L. F. Bosart, K. M. Bell, and F. J. Pereira, 2008: Use of normalized anomaly fields to anticipate extreme rainfall in the mountains of northern California. *Wea. Forecasting,* **23,** 336–356.

Kalnay, E., and Coauthors, 1996: The NCEP/NCAR 40-Year Reanalysis Project. *Bull. Amer. Meteor. Soc.,* **77,** 437–471.

Kiladis, G. N., 1998: Observations of Rossby waves linked to convection over the eastern tropical Pacific. *J. Atmos. Sci.,* **55,** 321–339.

——, and K. M. Weickmann, 1992: Extratropical forcing of tropical Pacific convection during northern winter. *Mon. Wea. Rev.,* **120,** 1924–1938.

——, M. C. Wheeler, P. T. Haertel, K. H. Straub, and P. E. Roundy, 2009: Convectively coupled equatorial waves. *Rev. Geophys.,* **47,** RG2003, doi:10.1029/2008RG000266.

Knippertz, P., and J. E. Martin, 2007: A Pacific moisture conveyor belt and its relationship to a significant precipitation event in the semiarid southwestern United States. *Wea. Forecasting,* **22,** 125–144.

——, and H. Wernli, 2010: A Lagrangian climatology of tropical moisture exports to the Northern Hemispheric extratropics. *J. Climate,* **23,** 987–1003.

Knutson, T. R., and K. M. Weickmann, 1987: 30–60 day atmospheric oscillations: Composite life cycles of convection and circulation anomalies. *Mon. Wea. Rev.,* **115,** 1407–1436.

Leung, L. R., and Y. Qian, 2009: Atmospheric rivers induced heavy precipitation and flooding in the western U.S. simulated by the WRF regional climate model. *Geophys. Res. Lett.,* **36,** L03820, doi:10.1029/2008GL036445.

Ma, Z., W. Y.-H. Kuo, F. M. Ralph, P. J. Neiman, G. A. Wick, E. Sukovich, and B. Wang, 2011: Assimilation of GPS radio occultation data for an intense atmospheric river with the NCEP Regional GSI system. *Mon. Wea. Rev.,* in press.

Matthews, A. J., and G. N. Kiladis, 1999: The tropical–extratropical interaction between high-frequency transients and the Madden–Julian oscillation. *Mon. Wea. Rev.,* **127,** 661–677.

Mattioli, V., E. R. Westwater, C. Cimini, J. S. Liljegren, B. M. Lesht, S. I. Gutman, and F. J. Schmidlin, 2007: Analysis of radiosonde and ground-based remotely sensed PWV data from the 2004 North Slope of Alaska Arctic Winter Radiometric Experiment. *J. Atmos. Oceanic Technol.,* **24,** 415–431.

Mo, K. C., 1999: Alternating wet and dry episodes over California and intraseasonal oscillations. *Mon. Wea. Rev.,* **127,** 2759–2776.

——, and R. W. Higgins, 1998a: Tropical convection and precipitation regimes in the western United States. *J. Climate,* **11,** 2404–2423.

——, and ——, 1998b: Tropical influences on California precipitation. *J. Climate,* **11,** 412–430.

Morss, R. E., and F. M. Ralph, 2007: Use of information by National Weather Service forecasters and emergency managers during CALJET and PACJET-2001. *Wea. Forecasting,* **22,** 539–555.

Neiman, P. J., and M. A. Shapiro, 1989: Retrieving horizontal temperature gradients and advections from single-station wind profiler observations. *Wea. Forecasting,* **4,** 222–233.

——, F. M. Ralph, A. B. White, D. E. Kingsmill, and P. O. G. Persson, 2002: The statistical relationship between upslope flow and rainfall in California's coastal mountains: Observations during CALJET. *Mon. Wea. Rev.,* **130,** 1468–1492.

——, P. O. G. Persson, F. M. Ralph, D. P. Jorgensen, A. B. White, and D. A. Kingsmill, 2004: Modification of fronts and precipitation by coastal blocking during an intense landfalling winter storm in southern California: Observations during CALJET. *Mon. Wea. Rev.,* **132,** 242–273.

——, F. M. Ralph, G. A. Wick, Y.-H. Kuo, T.-K. Wee, Z. Ma, G. H. Taylor, and M. D. Dettinger, 2008a: Diagnosis of an intense atmospheric river impacting the Pacific Northwest: Storm summary and offshore vertical structure observed with COSMIC satellite retrievals. *Mon. Wea. Rev.,* **136,** 4398–4420.

——, ——, ——, J. Lundquist, and M. D. Dettinger, 2008b: Meteorological characteristics and overland precipitation impacts of atmospheric rivers affecting the west coast of North America based on eight years of SSM/I satellite observations. *J. Hydrometeor.,* **9,** 22–47.

——, A. B. White, F. M. Ralph, D. J. Gottas, and S. I. Gutman, 2009: A water vapor flux tool for precipitation forecasting. *Water Manage.,* **162,** 83–94.

Persson, P. O. G., P. J. Neiman, B. Walter, J.-W. Bao, and F. M. Ralph, 2005: Contributions from California coastal-zone surface fluxes to heavy coastal precipitation: A CALJET case study during the strong El Niño of 1998. *Mon. Wea. Rev.,* **133,** 1175–1198.

Ralph, F. M., P. J. Neiman, D. E. Kingsmill, P. O. G. Persson, A. B. White, E. T. Strem, E. D. Andrews, and R. C. Antweiler, 2003: The impact of a prominent rain shadow on flooding in California's Santa Cruz mountains: A CALJET case study and sensitivity to the ENSO cycle. *J. Hydrometeor.,* **4,** 1243–1264.

——, ——, and G. A. Wick, 2004: Satellite and CALJET aircraft observations of atmospheric rivers over the eastern North Pacific Ocean during the winter of 1997/98. *Mon. Wea. Rev.,* **132,** 1721–1745.

——, ——, and R. Rotunno, 2005a: Dropsonde observations in low-level jets over the northeastern Pacific Ocean from CALJET-1998 and PACJET-2001: Mean vertical-profile and atmospheric-river characteristics. *Mon. Wea. Rev.,* **133,** 889–910.

——, and Coauthors, 2005b: Improving short-term (0-48 h) cool-season quantitative precipitation forecasting: Recommendations from a USWRP workshop. *Bull. Amer. Meteor. Soc.,* **86,** 1619–1632.

——, P. J. Neiman, G. A. Wick, S. I. Gutman, M. D. Dettinger, D. R. Cayan, and A. B. White, 2006: Flooding on California's Russian River: Role of atmospheric rivers. *Geophys. Res. Lett.,* **33,** L13801, doi:10.1029/2006GL026689.

——, E. Sukovich, D. Reynolds, M. Dettinger, S. Weagle, W. Clark, and P. J. Neiman, 2010: Assessment of extreme quantitative precipitation forecasts and development of regional extreme event thresholds using data from HMT-2006 and COOP observers. *J. Hydrometeor.,* **11,** 1286–1304.

Schluessel, P., and W. J. Emery, 1990: Atmospheric water vapour over oceans from SSM/I measurements. *Int. J. Remote Sens.,* **11,** 753–766.

Shapiro, M. A., H. Wernli, N. A. Bond, and R. Langland, 2001: The influence of the 1997–1999 El Niño–Southern Oscillation on extratropical baroclinic life cycles over the eastern North Pacific. *Quart. J. Roy. Meteor. Soc.,* **127,** 331–342.

Smith, B. L., S. E. Yuter, P. J. Neiman, and D. E. Kingsmill, 2010: Water vapor fluxes and orographic precipitation over northern California associated with a land-falling atmospheric river. *Mon. Wea. Rev.,* **138,** 74–100.

Stohl, A., C. Forster, and H. Sodemann, 2008: Remote sources of water vapor forming precipitation on the Norwegian west coast at 60°N—A tale of hurricanes and an atmospheric river. *J. Geophys. Res.,* **113,** D05102, doi:10.1029/2007JD009006.

Toth, Z., O. Talagrand, and Y. Zhu, 2005: The attributes of forecast systems: A framework for the evaluation and calibration of weather forecasts. *Predictability of Weather and Climate,* T. N. Palmer and R. Hagedorn, Eds., Cambridge University Press, 584–595.

Weber, B. L., D. B. Wuertz, D. C. Welsh, and R. McPeek, 1993: Quality controls for profiler measurements of winds and RASS temperatures. *J. Atmos. Oceanic Technol.,* **10,** 452–464.

Weng, F., and N. C. Grody, 1994: Retrieval of cloud liquid water using the Special Sensor Microwave Imager. *J. Geophys. Res.,* **99,** 25 535–25 551.

Wentz, F. J., 1995: The intercomparison of 53 SSM/I water vapor algorithms. Remote Sensing Systems Tech. Rep., Santa Rosa, CA, 19 pp.

Wheeler, M., and K. M. Weickmann, 2001: Real-time monitoring and prediction of modes of coherent synoptic to intraseasonal tropical variability. *Mon. Wea. Rev.,* **129,** 2677–2694.

——, and H. H. Hendon, 2004: An all-season real-time multivariate MJO index: Development of an index for monitoring and prediction. *Mon. Wea. Rev.,* **132,** 1917–1932.

——, G. N. Kiladis, and P. J. Webster, 2000: Large-scale dynamical fields associated with convectively coupled equatorial waves. *J. Atmos. Sci.,* **57,** 613–640.

White, A. B., D. J. Gottas, E. Strem, F. M. Ralph, and P. J. Neiman, 2002: An automated brightband height detection algorithm for use with Doppler radar vertical spectral moments. *J. Oceanic Atmos. Technol.,* **19,** 687–697.

Wratt, D. S., and Coauthors, 1996: The New Zealand Southern Alps Experiment. *Bull. Amer. Meteor. Soc.,* **77,** 683–692.

Yuan, H. J., J. A. McGinley, P. J. Schultz, C. J. Anderson, and C. Lu, 2008: Short-range precipitation forecasts from time-lagged multimodel ensembles during HMT-West 2006 field campaign. *J. Hydrometeor.,* **9,** 477–491.

Zhang, C., 2005: Madden–Julian oscillation. *Rev. Geophys.,* **43,** RG2003, doi:10.1029/2004RG000158.

Zhu, Y., and R. E. Newell, 1998: A proposed algorithm for moisture fluxes from atmospheric rivers. *Mon. Wea. Rev.,* **126,** 725–735.